https://doi.org/10.5194/egusphere-2026-5582
Preprint. Discussion started: 11 November 2026
© Author(s) 2026. CC BY 4.0 License.

Wave-induced atmosphere–ocean processes and their effects on Antarctic sea ice: A case study with an atmosphere–ocean–wave–sea ice coupled model

Chao-Yuan Yang[1], Jiping Liu[1], Xiaoqi Xu[2], Xiaoxu Shi[1], Hu Yang[1]

[1]Southern Marine Science and Engineering Guangdong Laboratory (Zhuhai) and School of Atmospheric Sciences, Sun Yat-sen University, Zhuhai, Guangdong, China

[2]Institute for Development and Programme Design, China Meteorological Administration, Beijing, China.

Corresponding authors:

Chao-Yuan Yang (yangchaoyuan@sml-zhuhai.cn) and Jiping Liu (liujp63@mail.sysu.edu.cn)

https://doi.org/10.5194/egusphere-2026-5582
Preprint. Discussion started: 11 November 2026
© Author(s) 2026. CC BY 4.0 License.

Abstract

Ocean waves are an important component of polar air–ocean–sea-ice interactions, but their indirect impacts on Antarctic sea ice through coupled atmosphere–ocean processes remain poorly understood. Here, we investigate the influence of wave-induced processes on Antarctic sea ice using a newly developed regional atmosphere–ocean–wave–sea-ice coupled model. The model incorporated two wave-induced processes that affect the ocean and atmosphere: spray-mediated turbulent heat fluxes and Langmuir turbulence-enhanced vertical mixing. A set of pan-Antarctic simulations is conducted during the 2002 sea-ice growth season, including an explosive cyclone event in the Ross Sea, with both atmosphere-nudged and fully coupled configurations used to examine the role of atmospheric feedbacks. Wave-induced processes modify sea ice through their effects on the upper-ocean thermal state and air–sea energy exchange. In the atmosphere-nudged configuration, wave-induced responses are relatively weak and spatially coherent, with enhanced oceanic heat loss and upper-ocean cooling contributing to a modest increase in sea-ice extent. In contrast, fully coupled simulations produce substantially stronger and more heterogeneous sea-ice responses. The inclusion of wave processes alters surface heat fluxes, which modify near-surface atmospheric stability and circulation, leading to feedbacks that amplify regional variability in ocean temperature and sea-ice conditions. The strongest responses occur near the Antarctic marginal ice zone, where wave penetration into partially ice-covered regions enhances spray-mediated heat loss and promotes local supercooling, favoring sea-ice formation. Our results demonstrate that ocean waves influence Antarctic sea ice not only through direct mechanical processes such as ice breakup, but also through indirect thermodynamic pathways involving air–sea exchange, upper-ocean mixing, and atmospheric circulation feedbacks. These results suggest that wave-related atmosphere–ocean–sea ice interactions represent a potentially important pathway affecting Antarctic sea-ice variability, motivating further investigation across different seasons, regions, and climate states.

https://doi.org/10.5194/egusphere-2026-5582
Preprint. Discussion started: 11 November 2026
© Author(s) 2026. CC BY 4.0 License.

1. Introduction

Antarctic sea ice has undergone a pronounced reorganization in recent years, shifting from the modest expansion with strong regional variability during much of the satellite era to repeated record-low conditions after 2016. This includes exceptionally low summer minima in 2017, 2022, and 2023 and persistent negative anomalies (Purich and Doddridge, 2023; Raphael et al., 2025). Concurrently, ocean wave activity has intensified in the Southern Ocean. Satellite altimetry, reanalysis, and ensemble analyses based on multiple ocean-wave products indicate upward trends in significant wave height and extreme wave conditions across large parts of the Southern Ocean, particularly in regions dominated by energetic winter storm (Young and Ribal, 2019; Erikson et al., 2022; Laloue et al., 2024). These concurrent changes are dynamically linked. Sea ice modulates wave growth and propagation by limiting fetch and attenuating wave energy, while ocean waves can fracture the marginal ice zone and accelerate ice-edge retreat. In a key observational study, Kohout et al. (2014) demonstrated that large storm-generated waves can propagate far into Antarctic sea ice and break ice hundreds of kilometers from the ice edge. This implies that recent increases Southern Ocean wave activity may amplify Antarctic sea-ice variability and should be explicitly considered when modeling these changes.

Ocean waves exert a first-order control on air–sea interaction by modifying both the atmospheric boundary condition and the upper-ocean turbulent structure. At the interface, the evolving sea state alters aerodynamic roughness and momentum transfer, given that surface roughness depends not only on wind speed but also on wave properties such as wave height, steepness, and age (Taylor and Yelland, 2001; Drennan et al., 2003). Under strong winds, wave breaking produces sea spray, whose droplets exchange heat and moisture with the marine atmospheric boundary layer, substantially affecting sensible and latent heat fluxes (Andreas, 1992; Andreas et al., 2015; Veron, 2015; Barr et al., 2023). Waves further influence the ocean interior by enhancing vertical mixing in the upper ocean. Breaking waves inject turbulent kinetic energy (TKE) directly into the near-surface layer, producing elevated dissipation beneath the surface and strengthening turbulent exchange across the mixed layer (Terray et al., 1996; D'Asaro, 2014). Nonbreaking waves also contribute to mixing through wave-turbulence

https://doi.org/10.5194/egusphere-2026-5582
Preprint. Discussion started: 11 November 2026
© Author(s) 2026. CC BY 4.0 License.

interactions, Stokes-drift-driven Langmuir turbulence, and orbital-motion-related turbulence, affecting mixed-layer depth, sea surface temperature (SST), and the vertical redistribution of heat and momentum (McWilliams et al., 1997; Qiao et al., 2004; Sullivan and McWilliams, 2010; Babanin and Haus, 2009). Thus, Southern Ocean waves affect Antarctic sea ice through multiple pathways: directly by promoting mechanical breakup, and indirectly by altering air–sea heat exchange and upper-ocean mixing, which shape the ocean energy budget that governs sea-ice growth and melt. This indirect pathway is also partly demonstrated by our recent Arctic coupled-modeling study (Yang et al., 2024), which showed that wave-related processes can influence sea-ice simulations through atmosphere-ocean interactions, in addition to their direct role in reducing floe size.

Several studies have begun to incorporate wave-related processes into coupled climate model or prediction systems, although most of them have emphasized air–sea exchange and upper-ocean responses rather than Antarctic sea ice itself. Li et al. (2016) coupled WAVEWATCH III to CESM and showed that Langmuir-turbulence parameterization, constrained by Stokes drift and wind–wave alignment, deepens and improves mixed-layer-depth simulations, with particularly large effects in the Southern Ocean. Song et al. (2022) demonstrated in FIO-ESM v2.0 that sea spray can substantially modify latent and sensible heat fluxes over the Southern Ocean, producing cooler SST, a more stable and moister lower atmosphere, and increased cloud cover—all relevant to the thermodynamic states controlling Antarctic sea ice. Similarly, Shi et al. (2022) implemented a CFSv2.0–WW3 coupled prediction system and evaluated multiple wave-related processes, including Langmuir mixing, Stokes–Coriolis forcing with entrainment, Stokes-drift-modified air-sea fluxes, and wave-dependent roughness length. They showed that these processes can reduce biases in SST, mixed-layer depth, near-surface air temperature, winds, and significant wave height. More targeted, though less fully coupled, Li et al. (2025) showed that wave-induced turbulence and wave-to-ice stress under wave–sea ice–ocean coupling can alter mixed-layer depth, ice growth and melt. Studies with direct wave–ice interactions have further demonstrated that the prognostic waves and sea ice floe size influence ice melting behavior, particularly the balance between basal and lateral

https://doi.org/10.5194/egusphere-2026-5582
Preprint. Discussion started: 11 November 2026
© Author(s) 2026. CC BY 4.0 License.

ice melting, during the melt season (e.g., Roach et al., 2019; Yang et al., 2024). Collectively, these studies demonstrated that waves influence Antarctic sea ice both indirectly through air–sea heat exchange and mixing, and directly through attenuation, ice fracture, and floe-size evolution.

In this paper, we present a newly developed atmosphere–ocean–wave–sea ice coupled model, in which we implement physical processes associated with spray-mediated heat flux and Langmuir mixing. Using this new coupled model, we investigate the wave effects on Antarctic sea ice focusing on the indirect atmospheric and oceanic pathways. This paper is structured as follows. Section 2 provides an overview of the coupled model, focusing on the newly implemented physical processes, and describes the experiment designs and the diagnostics. Section 3 examines the responses of sea ice to spray-mediated heat flux and Langmuir mixing in the atmosphere-nudged and fully-interactive configurations, and the mechanisms behind the responses. Discussions and concluding remarks are provided in Section 4.

2. Methods

2.1. The atmosphere–ocean–wave–sea ice coupled model

In this study, we employ a recently developed atmosphere–ocean–wave–sea ice coupled model for the Antarctic. It is built from the coupled model developed for investigating direct wave–ice interactions in the Arctic (Yang et al., 2024; hereafter Y24) with several modifications. First, an improved flux coupling approach to minimize energy inconsistency between the atmosphere and the ocean-sea ice components is implemented in the Y24 model (Yang et al., 2026). Second, the wave model component in the Y24 model is changed from the Simulating Waves Nearshore (SWAN) to WAVEWATCH III (WW3) to take advantage of its broader range of physics parameterizations, particularly those for wave–ice interactions. Third, Y24 considered changes in interfacial heat flux caused by a wave-roughened ocean surface (Taylor and Yelland, 2001) and wave-enhanced near-surface ocean mixing associated with TKE injection (Kumar et al., 2012). In the present study, we extend this framework by implementing sea spray-mediated heat flux and a modified K-profile parameterization (KPP)

https://doi.org/10.5194/egusphere-2026-5582
Preprint. Discussion started: 11 November 2026
© Author(s) 2026. CC BY 4.0 License.

that approximates the influence of Langmuir turbulence, and investigate the combined effects of these wave-related processes on Antarctic sea ice changes. Details of these newly implemented schemes are described in the following sections.

2.2. Spray-mediated heat flux

Following the work of Andreas et al. (2015; hereafter A15), we implement spray-mediated sensible and latent heat fluxes (Q_S and Q_L) for spray droplets with initial radius r_0, which can be described as

$$Q_S(r_0) = \rho_s c_{ps}(T_w - T_{eq})\left[1 - exp\left(-\tau_f/\tau_T\right)\right]\left(\frac{4\pi {r_0}^3}{3}\frac{dF}{dr_0}\right), \quad (1)$$

$$Q_L(r_0) = \rho_s L_v\left\{1 - \left[\frac{r(\tau_f)}{r_0}\right]^3\right\}\left(\frac{4\pi {r_0}^3}{3}\frac{dF}{dr_0}\right), \quad (2)$$

where ρ_s is the density of seawater, c_{ps} is the specific heat at constant pressure, L_v is the latent heat of vaporization, T_w is the initial temperature of spray droplets, which is equal to the sea surface temperature, T_{eq} is the equilibrium droplet temperature with the environment, τ_f is the residence time of droplets in the air associated with the wave height, τ_T is the e-folding time for temperature changes of droplets, $r(\tau_f)$ is the final radius of droplets before falling back to the ocean, and dF/dr_0 is the sea spray generation function (SSGF) for the volume of droplets with initial radius r_0. Details of variables in Eqs. (1)–(2) are described in A15. The total spray-mediated heat flux ($\overline{Q_S}$ and $\overline{Q_L}$) is obtained by integrating Eqs. (1)–(2) over all droplet radii. Total sensible and latent heat fluxes (H_S and H_L) between the atmosphere and the ocean are represented as

$$H_S = H_{S,int} + \overline{Q_S}, \quad (3)$$

$$H_L = H_{L,int} + \overline{Q_L}, \quad (4)$$

where $H_{S,int}$ and $H_{L,int}$ are the interfacial heat fluxes calculated by the Coupled Ocean–Atmosphere Response Experiment (COARE) 3.0 bulk formula (Fairall et al., 2003) originally implemented in the model described in Section 2.1.

For SSGF, we employ the formulation introduced by Zhao et al. (2024), which is expressed as a function of wind speed (U_{10}), wave age (β), and wave steepness (δ). The

https://doi.org/10.5194/egusphere-2026-5582
Preprint. Discussion started: 11 November 2026
© Author(s) 2026. CC BY 4.0 License.

formulations for bubble droplets ($r_0 < 20\ \mu m$) and spume droplets ($r_0 \geq 20\ \mu m$) are given by

$$dF/dr_0 = \begin{cases} 1.40 \times 10^1 {R_B}^{1.5} {r_0}^{-3.5}, & 2 \leq r_0 < 20\ \mu m \\ 7.84 \times 10^{-3} {R_B}^{1.5} {r_0}^{-1}, & 20 \leq r_0 < 75\ \mu m \\ 4.41 \times 10^1 {R_B}^{1.5} {r_0}^{-3}, & 75 \leq r_0 < 200\ \mu m \\ 1.41 \times 10^{13} {R_B}^{1.5} {r_0}^{-8}, & 200 \leq r_0 < 500\ \mu m \end{cases}, \quad (5)$$

where R_B is the windsea Reynolds number proposed by Toba et al. (2006), defined as

$$R_B = C_D \frac{{U_{10}}^3}{g\nu}\beta, \qquad \beta = \frac{g}{\omega_p U_{10}}, \quad (6)$$

Here, C_D is the drag coefficient, g is the gravitational acceleration, ν is the kinematic viscosity of air, and ω_p is the angular frequency at the spectral peak. For C_D, Zhao et al. (2024) adopt a linear parameterization introduced by Guan and Xie (2004), parameterized as

$$C_D = 1 \times 10^{-3}(0.78 + 0.475\delta^{0.5} U_{10}), \quad (7)$$

In addition, δ is defined as

$$\delta = \begin{cases} 3.21 \times 10^{-2}\beta^{-0.24}, & \beta > 0.4 \\ 0.04, & \beta \leq 0.4 \end{cases}, \quad (8)$$

2.3. Langmuir mixing

McWilliams and Sullivan (2000, hereafter MS00) introduced a modification to the widely used KPP vertical mixing scheme (Large et al., 1994) to account for vertical mixing induced by Langmuir turbulence. The key concept of MS00 is the introduction of a Langmuir enhancement factor (ε), which is a function of the turbulent Langmuir number (L_a), to enhance the turbulent velocity (w_x) in the KPP framework. This enhancement modifies the calculated values of the boundary-layer Richardson number, the eddy diffusivity, and the nonlocal flux term in the KPP scheme. Previous studies have adopted different definitions of L_a (e.g., McWilliams et al., 1997; Harcourt and D'Asaro, 2008; Van Roekel et al., 2012) and different scalings of w_x with ε (e.g., MS00; Smyth et al., 2002; Van Roekel et al., 2012).

In this study, we follow the formulation proposed by Wang et al. (2025), and define the scaled w_x as

$$w_x = \frac{\kappa u^*}{\phi_x}(1 + \varepsilon), \quad (9)$$

$$\varepsilon = {L_a}^{-2/3} C_{L_a}, \quad (10)$$

https://doi.org/10.5194/egusphere-2026-5582
Preprint. Discussion started: 11 November 2026
© Author(s) 2026. CC BY 4.0 License.

$$L_a = \sqrt{u^*/u^s}, \qquad (11)$$

$$C_{L_a} = 0.2(\cos\theta + 1), \qquad (12)$$

Here, κ is the von Kármán constant, u^* is the friction velocity in seawater, u^s is the surface Stokes drift, ϕ_x is the Monin–Obukhov similarity function for momentum and scalar, L_a follows the definition of McWilliams et al. (1997), and C_{L_a} is an empirical function representing the misalignment angle θ between waves and winds.

2.4. Wave radiation stress and other changes to the Y24 model

The Y24 model accounts for the attenuation of wave energy by sea ice, but the wave energy removed by this attenuation is not explicitly transferred to sea ice or otherwise represented as a physical effect in the coupled system. Wave attenuation is also accompanied by a loss of wave momentum. As described in Boutin et al. (2020), when waves are attenuated by dissipation or scattering, the associated momentum loss is transferred to the medium responsible for the attenuation. In case of sea ice, this momentum transfer acts as wave radiation stress (WRS) that drives the ice in the direction of wave propagation. This process is implemented by coupling the WRS computed by WW3 to CICE, where it is incorporated as an additional term in the sea-ice momentum equation. In addition to the wave-related processes described above, we also implement an ice–ocean heat flux parameterization that accounts for the local salinity equilibrium associated with meltwater from sea ice (Notz et al., 2003; Shi et al., 2021).

2.5. Model setup and experiment designs

In this study, the WRF, ROMS, WW3, and CICE model components use the same model grid with 450 x 450 grid points in the x- and y-directions, respectively, and a horizontal resolution of ~24 km over the region south of 40°S in the polar stereographic projection (see Fig. S1 in the Supplementary). Initial and lateral boundary conditions for WRF are derived from the fifth-generation of European Centre for Medium-Range Weather Forecasts Reanalysis (ERA5, Hersbach et al., 2023), with a 6-hour temporal resolution and a spatial resolution of 0.25 degrees. The final optimized state estimate, Cube92, from the Estimating the Circulation and Climate of the Ocean, Phase II (ECCO2; Menemenlis et al., 2008) is used to provide initial

https://doi.org/10.5194/egusphere-2026-5582
Preprint. Discussion started: 11 November 2026
© Author(s) 2026. CC BY 4.0 License.

and open boundary conditions for ROMS and CICE.

As in Y24, the vortex force (VF) formulation for wave effects on ocean currents (Uchiyama et al., 2010) is employed in this study. In this formulation, the Stokes velocity is derived from a monochromatic wave field, and its surface component is used in Eq. (11) to calculate the turbulent Langmuir number. The Generic Length-Scale scheme (Umlauf and Burchard, 2003) used in Y24 to represent TKE injection into the surface layer from surface wave breaking (Kumar et al., 2012) is replaced by the modified KPP scheme described in Section 2.3. The mixing induced by breaking waves is then represented using the same approach as in the VF formulation. Physical parameterizations for each model component follow those in Y24, with several modifications, particularly for the newly introduced wave component (WW3), as summarized in Table 1.

Table 1 The summary of physic parameterizations used in all simulations.

WRF physics	
Cumulus	Grell-Freitas (Freitas et al. 2018)
Microphysics	Morrison 2-moment (Morrison et al. 2009)
Longwave radiation	CAM spectral band scheme (Collins et al. 2004)
Shortwave radiation	CAM spectral band scheme (Collins et al. 2004)
Boundary layer	MYNN (Nakanishi and Niino, 2009)
Land surface	Unified Noah LSM (Chen and Dudhia, 2001)
ROMS physics	
Tracer advection	Upwind third-order horizontal advection (Shchepetkin, and McWilliams, 2005) Centered fourth-order vertical advection (Shchepetkin, and McWilliams, 2005)
Tracer vertical mixing	KPP (Large et al., 1994) with modifications
CICE physics	
Ice dynamics	EVP (Hunke and Dukowicz, 1997)
Ice thermodynamics	Mushy-layer (Turner et al., 2013)
Shortwave albedo	Delta-Eddington (Briegleb and Light, 2007)
Meltpond	Level-ice (Hunke et al., 2013)
WW3 physics switches	
Wind source and wave breaking	ST4 (Ardhuin et al., 2010)
Bottom friction	BT4 (Ardhuin et al., 2003)
Nonlinear interactions	NL1 (Hasselmann et al., 1985)
Linear input	LN1 (Cavaleri and Malanotte-Rizzoli, 1981; Tolman, 1992)
Energy reflection	REF1 (Ardhuin and Roland, 2012)
Depth-induced breaking	DB1 (Battjes and Janssen, 1978)

https://doi.org/10.5194/egusphere-2026-5582
Preprint. Discussion started: 11 November 2026
© Author(s) 2026. CC BY 4.0 License.

Triad interactions	TR0 (deactivated)
Bottom scattering	BS0 (deactivated)
Sea ice damping	IC4M3 (Horvat and Tziperman, 2015)
Sea ice scattering	IS0 (deactivated)

A set of numerical experiments is conducted for the period from 00:00 UTC 22 April 2002 to 00:00 UTC 1 September 2002 to investigate the effects of wave-induced processes on Antarctic sea ice. This period includes an explosive cyclone (EC) that developed and intensified between 24 and 30 April 2002 over open-water regions of the Ross Sea (Xu et al., 2025, hereafter EC02), providing strong forcing for wave development. Specifically, the control experiment (CTRL) excludes the spray-mediated heat flux and Langmuir mixing described in Sections 2.2–2.3, whereas the full-effect experiment (FULL) includes both processes. The parameterizations described in Section 2.4, particularly the wave radiation stress (WRS), are included in both experiments, as the primary objective of this study is to examine how ocean waves influence sea ice through atmospheric and oceanic pathways. Based on these experiments, two configurations are designed. In the first configuration, fully coupled interactions among the atmosphere, ocean, wave, and sea-ice components are allowed; this configuration is hereafter referred to as FREE configuration. In the second configuration, the three-dimensional atmospheric circulation is constrained using the WRF nudging scheme with ERA5 data; this configuration is hereafter referred to as NUD configuration. The latter configuration dynamically decouples the atmosphere from the other model components, thereby providing an analogue for ocean–wave–sea ice coupling with limited atmospheric thermodynamic response. Table 2 summarizes the details of these experiments and corresponding names derived from the combinations of CTRL/FULL and FREE/NUD.

Table 2 The summary of the experiments conducted in this study. SP: spray-mediated heat flux. LM: Langmuir mixing.

Experiment	Physics	Interactions
Exp_CTRL$_{FREE}$	No SP and LM	Full interactions
Exp_FULL$_{FREE}$	With SP and LM	Full interactions
Exp_CTRL$_{NUD}$	No SP and LM	Winds nudged in WRF
Exp_FULL$_{NUD}$	With SP and LM	Winds nudged in WRF

https://doi.org/10.5194/egusphere-2026-5582
Preprint. Discussion started: 11 November 2026
© Author(s) 2026. CC BY 4.0 License.

2.6. Diagnostics of sea surface temperature tendency

The ROMS model includes an online diagnostic module that computes temperature and salinity tendencies. This module diagnoses the individual contributions to tracer tendencies at each time step and outputs time-averaged values over a user-specified interval. In this study, we focus on the sea surface temperature (SST) tendency, for which the diagnosed equation can be written as

$$\left.\frac{\partial SST}{\partial t}\right|_{TOTAL} = \left.\frac{\partial SST}{\partial t}\right|_{HADV} + \left.\frac{\partial SST}{\partial t}\right|_{VADV} + \left.\frac{\partial SST}{\partial t}\right|_{HDIF} + \left.\frac{\partial SST}{\partial t}\right|_{VDIF}, \quad (13)$$

The terms on the right-hand side of Eq. (13) represent horizontal advection, vertical advection, horizontal diffusion, and vertical diffusion. The vertical diffusion term includes contributions from both net surface heat flux and vertical mixing. Spray-mediated heat flux modifies net surface heat flux, while Langmuir turbulence alters vertical mixing through the modified KPP scheme. To distinguish these effects, we further decompose the vertical diffusion term based on the daily mean outputs as follows:

$$\left.\frac{\partial SST}{\partial t}\right|_{VDIF} \approx \left.\frac{\partial SST}{\partial t}\right|_{SHF} + \left.\frac{\partial SST}{\partial t}\right|_{MIX}, \quad (14)$$

$$\left.\frac{\partial SST}{\partial t}\right|_{SHF} = \frac{F_{SHF} - F_{NSW} + A_{top}F_{NSW}}{\rho_s c_p \Delta z_{top}}, \quad (15)$$

Here, F_{SHF} is the net surface heat flux at the ocean surface, F_{NSW} is the net shortwave radiation at the ocean surface, A_{top} is the fraction of shortwave radiation absorbed within the top ocean layer, and Δz_{top} is the thickness of the top ocean layer. A_{top} is determined from the exponential decay of penetrating shortwave radiation with depth. The vertical mixing term includes both downgradient local mixing and nonlocal fluxes. However, these components are not explicitly available in standard ROMS outputs, since local mixing is computed implicitly. Therefore, the vertical mixing term is diagnosed as the residual after removing the contribution of net surface heat flux from the vertical mixing term.

3. Results

To examine the effects of spray-mediated heat fluxes and Langmuir mixing, we first focus on the developed wave state induced by EC02 on 27 April 2002 in the NUD configuration,

https://doi.org/10.5194/egusphere-2026-5582
Preprint. Discussion started: 11 November 2026
© Author(s) 2026. CC BY 4.0 License.

Exp_CTRL$_{NUD}$ and Exp_FULL$_{NUD}$. Figure 1 shows atmospheric circulation, wave conditions, and spray-mediated heat fluxes from Exp_FULL$_{NUD}$, together with the responses of near-surface variables and upper-ocean profiles to wave-related processes. Unless otherwise noted, "response" throughout this study denotes the difference between the FULL experiment and the corresponding CTRL experiment, separately for the NUD and FREE configurations. The full life cycle of EC02 in the NUD configuration is provided in Figures S2 and S3 in the Supplementary.

The calculated spray-mediated heat fluxes indicate that both sensible and latent heat fluxes associated with sea spray primarily transfer energy from the ocean to the atmosphere, with the latent component having a larger magnitude than the sensible component (Figs. 1c–d). Regions of stronger spray-mediated fluxes coincide with greater wave heights, reflecting enhanced spray generation and longer airborne residence time of spray droplets under higher-wave conditions (Fig. 1b). Although the spray-mediated heat fluxes generally act to transfer energy to the atmosphere, the responses of total turbulent heat fluxes exhibit more complex behavior. The response in total sensible heat flux (Fig. 1e) shows reduced upward heat transfer in regions of high-wave conditions, though enhanced upward heat transfer occurs near the ice edge associated with cold-air advection from the ice surface over the ocean surface (Fig. 1a). The response in total latent heat flux (Fig. 1f) is mainly characterized by enhanced upward heat transfer, with a spatial pattern similar to that of the spray-mediated latent heat flux shown in Figure 1d, but with a smaller magnitude.

As shown in Eqs. (3)–(4), the total turbulent heat fluxes include spray-mediated and interfacial components. The initially enhanced energy transfer from the ocean to the atmosphere through spray-mediated fluxes modifies the near-surface thermodynamic states, resulting in warmer and moister near-surface air and colder SST (Figs. 1h–j). These responses reduce the air–sea thermodynamic contrast and subsequently alter the interfacial fluxes. For sensible heat flux, the interfacial component acts to compensate for the spray-mediated flux, leading to a weaker response in total sensible heat flux than expected from the spray contribution alone. In contrast, the spray-mediated latent heat flux remains the dominant

https://doi.org/10.5194/egusphere-2026-5582
Preprint. Discussion started: 11 November 2026
© Author(s) 2026. CC BY 4.0 License.

contribution, so the total latent heat flux response largely follows its spatial pattern but with a reduced magnitude due to the opposing interfacial adjustment. Together, these compensating interfacial responses make the total turbulent heat flux response nonlinear with respect to the spray-mediated contribution.

The response associated with vertical mixing depends on three-dimensional ocean state. Therefore, two regions with local maxima in wave height, indicated by the blue box (160°-170°W, 52.5°S-62.5°S) and the red box (145°W-115°W, 50°S-60°S) in Figure 1b, are selected for averaging upper-ocean profiles over the upper 150 m (Figs. 1k–n). For temperature, Exp_FULL_{NUD} shows slightly colder profiles than Exp_CTRL_{NUD} by approximately 0.02-0.04°C in the upper 0-80 m layer in both boxes (Fig. 1k–l), with slightly larger cooling response in the blue box. For temperature diffusivity, used here as a measure of mixing strength, both boxes show enhanced mixing in the upper 0-80 m layer (Figs. 1m–n), and the red box shows stronger enhancement. The larger mixing enhancement in the red box is consistent with the stronger wave forcing there, where a larger fraction of the area is characterized by wave heights exceeding 7 m compared with the blue box (Fig. 1b).

https://doi.org/10.5194/egusphere-2026-5582
Preprint. Discussion started: 11 November 2026
© Author(s) 2026. CC BY 4.0 License.

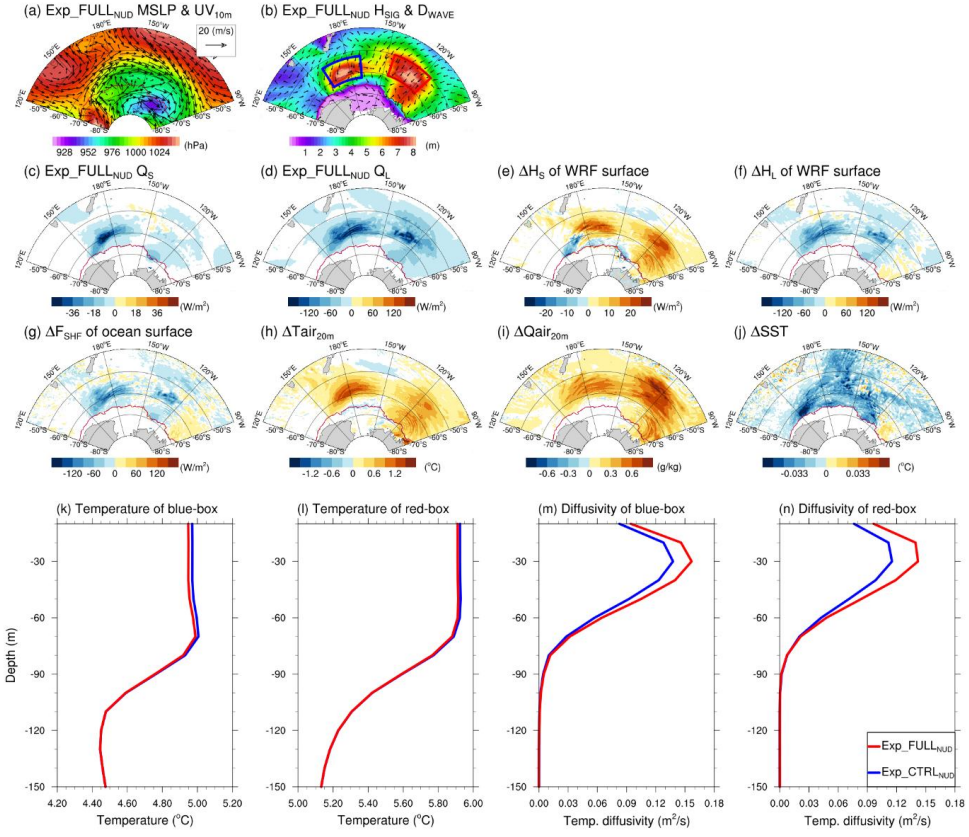


Figure 1 Atmospheric, wave, and oceanic conditions on 27 April 2002 in the Ross Sea. Panels show (a) atmospheric circulation, (b) wave conditions, (c) spray-mediated sensible heat flux, and (d) spray-mediated latent heat flux in Exp_FULL$_{NUD}$. Panels show the responses, defined as Exp_FULL$_{NUD}$ minus Exp_CTRL$_{NUD}$, in (e) total sensible heat flux, (f) total latent heat flux at the WRF lower boundary, (g) net ocean surface flux, (h) 20-m air temperature, (i) 20-m specific humidity, and (j) sea surface temperature. Panels show (k, l) upper-ocean temperature and (m, n) upper-ocean diffusivity for Exp_CTRL$_{NUD}$ (blue) and Exp_FULL$_{NUD}$ (red) in the blue and red boxes. All fluxes are defined as positive downward. Color ranges in panels showing responses were determined from the 99th percentile of the absolute magnitude.

It appears that sea ice responses are not readily apparent during the life cycle of EC02. As shown in Y24, the indirect effects of ocean waves on sea-ice changes require a longer time to emerge. Therefore, in this section, we examine the full simulation period of all experiments listed in Table 2, and shift from a Ross Sea-focused analysis to a Southern Ocean-wide perspective. Figure 2 shows the evolution of sea ice extent (SIE) and regional sea ice extent

https://doi.org/10.5194/egusphere-2026-5582
Preprint. Discussion started: 11 November 2026
© Author(s) 2026. CC BY 4.0 License.

(RSIE) across all experiments, as well as the responses of SIE and RSIE for both configurations. Here, SIE is defined as the total area of grid cells with a sea ice concentration (SIC) of at least 15%, whereas RSIE is presented as a Hovmöller diagram and is calculated by summing, within each 5° longitude band, the areas of grid cells exceeding the 15% SIC threshold. This representation highlights both the spatial and temporal variability of sea ice across different regions. At the pan-Antarctic scale, SIE in Exp_FULL$_{NUD}$ remains larger than that in Exp_CTRL$_{NUD}$ throughout the simulation. The difference is negligible until late-June, after which it increases to approximately $2 \times 10^5\ km^2$ (Figs. 2a–b, dashed lines). In contrast, the FREE configuration, Exp_CTRL$_{FREE}$ and Exp_FULL$_{FREE}$, exhibit a time-varying SIE response: SIE in Exp_FULL$_{FREE}$ is larger than that in Exp_CTRL$_{FREE}$ in May, but becomes smaller thereafter. Moreover, the magnitude of the SIE response in the FREE configuration reaches up to $4 \times 10^5\ km^2$, larger than that in the NUD configuration (Figs. 2a–b, solid lines). At the regional scale, RSIE in Exp_FULL$_{NUD}$ is generally larger than that in Exp_CTRL$_{NUD}$, with the largest response occurring in the 0°–60°E sector of the Southern Ocean, i.e., the eastern Weddell Sea and western Indian Ocean sector following the definition of Parkinson (2019) (Fig. 2d). The RSIE response in the 0°–60°E sector also increases after mid-June, contributing to the pan-Antarctic SIE response shown in Fig. 2b. Similar to SIE responses in the FREE configuration, RSIE also exhibits zonally varying responses, including a pronounced decrease in the eastern Weddell Sea and a pronounced increase in western Indian Ocean sector after June. The magnitude of the RSIE response in the FREE configuration is larger than that in the NUD configuration by approximately a factor of seven (Figs. 2d, f).

https://doi.org/10.5194/egusphere-2026-5582
Preprint. Discussion started: 11 November 2026
© Author(s) 2026. CC BY 4.0 License.

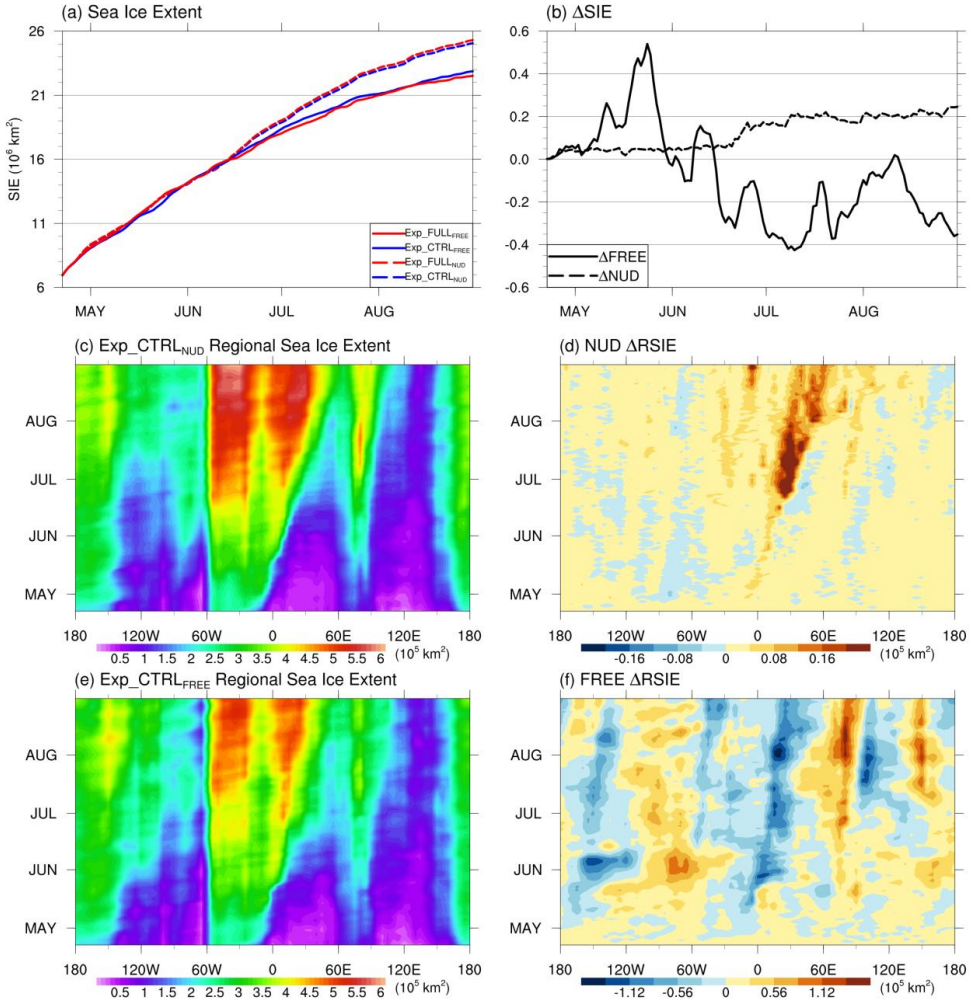


Figure 2 Sea ice evolution in all experiments. Panel (a) shows the total sea ice extent for Exp_CTRL$_{NUD}$ (blue, dashed), Exp_FULL$_{NUD}$ (red, dashed), Exp_CTRL$_{FREE}$ (blue, solid), and Exp_FULL$_{FREE}$ (red, solid). Panel (b) shows the responses in total sea ice extent for NUD (dashed) and FREE (solid) configurations. Panels show regional sea ice extent for (c) Exp_CTRL$_{NUD}$ and (e) Exp_CTRL$_{FREE}$, respectively. Panels show the responses in regional sea ice extent, defined as (d) Exp_FULL$_{NUD}$ minus Exp_CTRL$_{NUD}$ (f) and Exp_FULL$_{FREE}$ minus Exp_CTRL$_{FREE}$, respectively. Color ranges in panels (d, f) were determined from the 99th percentile of the absolute magnitude. For NUD-FREE paired variables, ranges were constrained to zero-symmetric integer multiples of a common reference scale.

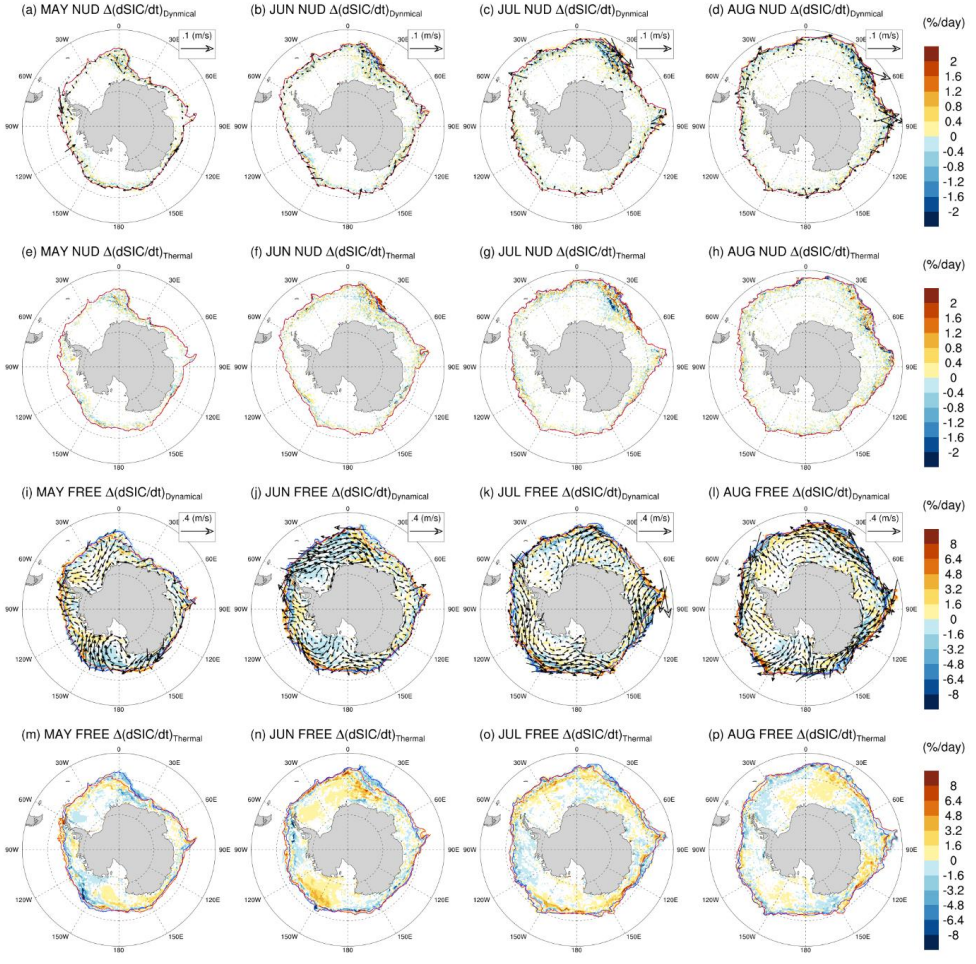
To quantify physical contributors to the SIE and RSIE responses shown in Fig. 2, we analyze the SIC tendency diagnostics from the CICE output, which decompose SIC changes

https://doi.org/10.5194/egusphere-2026-5582
Preprint. Discussion started: 11 November 2026
© Author(s) 2026. CC BY 4.0 License.

into dynamical and thermal contributions. Figure 3 presents the responses of the dynamical and thermal SIC tendencies from May to August, together with the CTRL and FULL ice-edge positions. Both dynamical and thermal SIC tendencies in the NUD configuration, that constrains atmospheric circulation, exhibit minor responses in high ice-concentration regions, but relatively stronger responses near the ice edge (Figs. 3a–h). In the 0°–60°E sector, where the largest RSIE response develops after mid-June (Fig. 2d; see Fig. S4 for a regional view), the initial response in June features dynamically induced SIC decreases on the higher-SIC side of the ice-edge and thermally induced SIC increases near and outside the ice edge (Figs. 3b, 3f, S4b, and S4f). Subsequently, the thermally induced SIC increase becomes increasingly confined to the ice-covered side of the 15% SIC contour, whereas dynamical response extends farther outward beyond the ice edge, consistent with the continued outward expansion of the ice edge and the associated increase in RSIE (Figs. 3c–d, 3g–h, S4c–d, and S4g–h). In contrast, the SIC tendency responses in the FREE configuration are approximately four times as large as those in the NUD configuration, occurring not only near the ice-edge but also within the interior pack ice (Figs. 3i–p). The differences in ice-edge position between Exp_CTRL_{FREE} and Exp_FULL_{FREE} might arise from the combined effects of dynamical and thermal processes, i.e., for the pronounced RSIE response in the eastern Weddell Sea in June shown in Fig. 2, dynamical processes enhance southwestward SIC transport, and thermal processes act to reduce SIC; together, these processes maintain open-water areas in the eastern Weddell Sea and thereby enhance the RSIE response. In addition to SIC tendencies, the responses in sea-ice volume (SIV) budget (Notz et al., 2016) are compared between the NUD and FREE configurations (Fig. S5 in the Supplementary). In the NUD configuration, the response in total SIV change increases after late June, broadly coinciding with the increasing SIE response (Fig. 2b), and is primarily associated with enhanced basal growth (Fig. S5d). In contrast, the FREE configuration exhibits SIV-budget responses that are an order of magnitude larger and considerably more variable than those in the NUD configuration. The total SIV-change response becomes strongly negative in late June, weakens toward near-neutral conditions through much of July, and turns predominantly positive in August. The late-June decrease is

https://doi.org/10.5194/egusphere-2026-5582
Preprint. Discussion started: 11 November 2026
© Author(s) 2026. CC BY 4.0 License.

388 associated mainly with reduced basal growth and enhanced oceanic melt, both of which favor
389 SIV loss, while their relative contributions and compensation by the other thermodynamics
390 processes vary substantially thereafter (Fig. S5).
391



392

393 Figure 3 Monthly mean responses of sea ice concentration (SIC) tendencies, defined as FULL
394 minus CTRL, from May to August. Panels show dynamical tendency responses (a–d) for the
395 NUD configuration and (i–l) for the FREE configuration. Panels show thermal tendency
396 responses (e–h) for the NUD configuration and (m–p) for the FREE configuration. The 15%
397 SIC contours from the CTRL experiment (blue) and the FULL experiment (red) are overlaid
398 on each panel. Arrows in the dynamical-tendency panels indicate the monthly mean sea-ice
399 motion responses, defined as FULL minus CTRL. Color ranges were determined from the 99th
400 percentile of the absolute magnitude. For NUD-FREE paired variables, ranges were

https://doi.org/10.5194/egusphere-2026-5582
Preprint. Discussion started: 11 November 2026
© Author(s) 2026. CC BY 4.0 License.

constrained to zero-symmetric integer multiples of a common reference scale.

Using the same monthly layout and ice-edge definition as in Figure 3, Figure 4 shows the corresponding SST responses in the NUD and FREE configurations. Overall, the differences in the ice-edge between the CTRL and FULL experiments are broadly consistent with the SST responses, with cooling associated with expanded ice-covered areas and warming associated with reduced ice cover. Nevertheless, the SST responses are not restricted to the non-overlapping ice-covered regions between the CTRL and FULL experiments, but extend farther north over the open ocean. In the NUD configuration, the SST responses display general cooling across the entire Southern Ocean (Figs. 4a–d), whereas in the FREE configuration, they exhibit zonally varying patterns of cooling and warming (Figs. 4e–h). The magnitude of SST responses in the NUD configuration is about one-sixth of that in the FREE configuration.

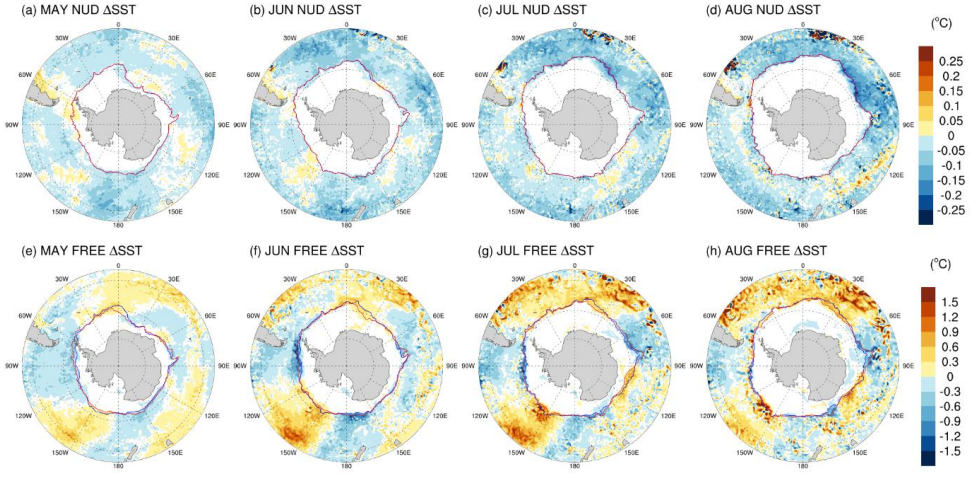


Figure 4 Monthly mean responses of sea surface temperature (SST), defined as FULL minus CTRL, from May to August. Panels show SST responses (a–d) for the NUD configuration, and (e–h) for the FREE configuration. The 15% sea ice concentration contours from the CTRL experiment (blue) and the FULL experiment (red) are overlaid on each panel. Color ranges were determined from the 99th percentile of the absolute magnitude. For NUD-FREE paired variables, ranges were constrained to zero-symmetric integer multiples of a common reference scale.

https://doi.org/10.5194/egusphere-2026-5582
Preprint. Discussion started: 11 November 2026
© Author(s) 2026. CC BY 4.0 License.

Figure 5 presents the responses of net ocean surface heat flux (F_{SHF}) in the NUD and FREE configurations, together with the spray-mediated heat flux in the FULL experiments. In the NUD configuration, the F_{SHF} response is predominantly upward over much of the open ocean (Figs. 5a–d), broadly consistent with the widespread SST cooling (Figs. 4a–d). In the FREE configuration, both the magnitude and spatial variability of the F_{SHF} response are considerably greater, with alternating regions of enhanced upward and downward heat transfer (Figs. 5i–l). Although some of the F_{SHF} responses locally coincide with the SST responses, their spatial correspondence is not systematic, indicating that the SST response cannot be interpreted solely from the local F_{SHF} response at the same time. Despite the much weaker F_{SHF} response in the NUD configuration, the spray-mediated heat fluxes near the ice edge are of comparable magnitude in the two configurations (Figs. 5e–h, 5m–p). This contrast is consistent with the compensating adjustment of the interfacial air–sea fluxes discussed previously, which prevents the total surface heat-flux response from scaling directly with the spray-mediated contribution. Nonzero spray-mediated heat fluxes also extend inside the ice edge in the NUD configuration, indicating wave penetration into partially ice-covered regions because spray-mediated fluxes are only calculated where significant wave height is nonzero. These fluxes overlap with regions of positive thermal SIC tendencies and enhanced RSIE responses (Figs. 2d, 3f–h, 5f–h). Because the near-surface ocean beneath sea ice remains close to the freezing point, the associated additional upward heat loss may favor local supercooling and subsequent frazil-ice formation (Fig. S5e).

https://doi.org/10.5194/egusphere-2026-5582
Preprint. Discussion started: 11 November 2026
© Author(s) 2026. CC BY 4.0 License.

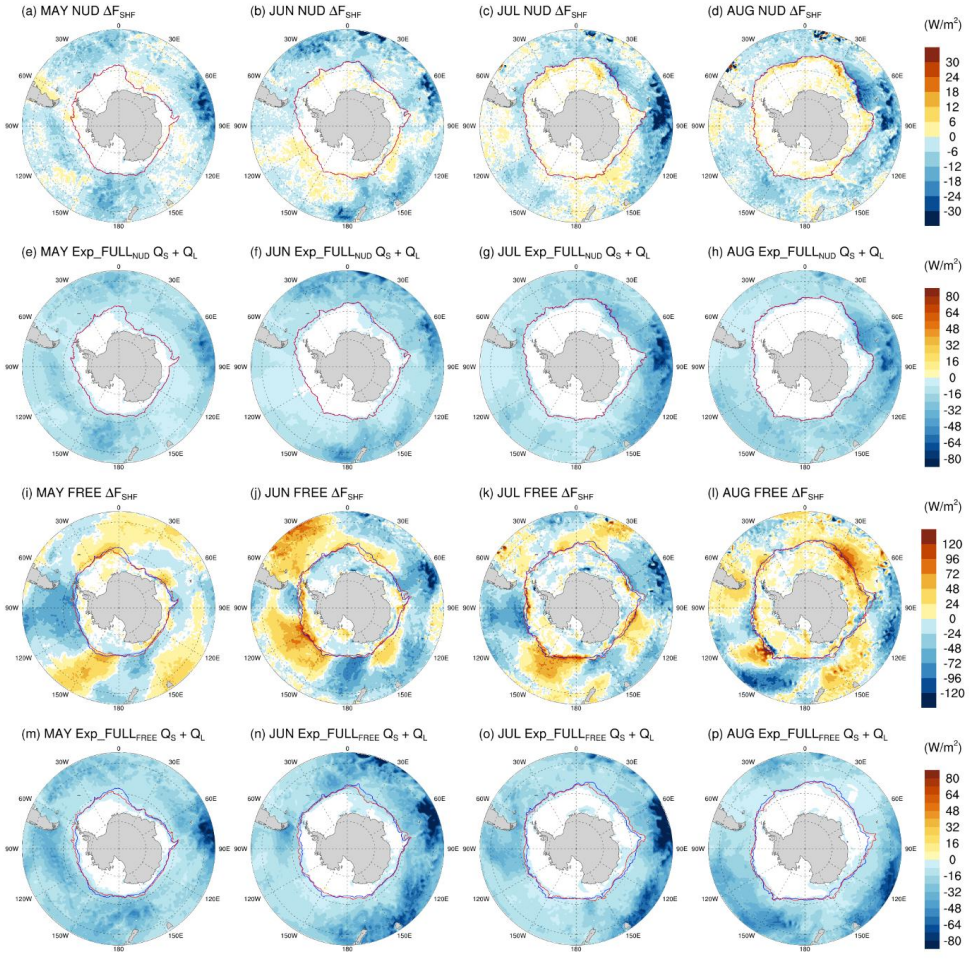
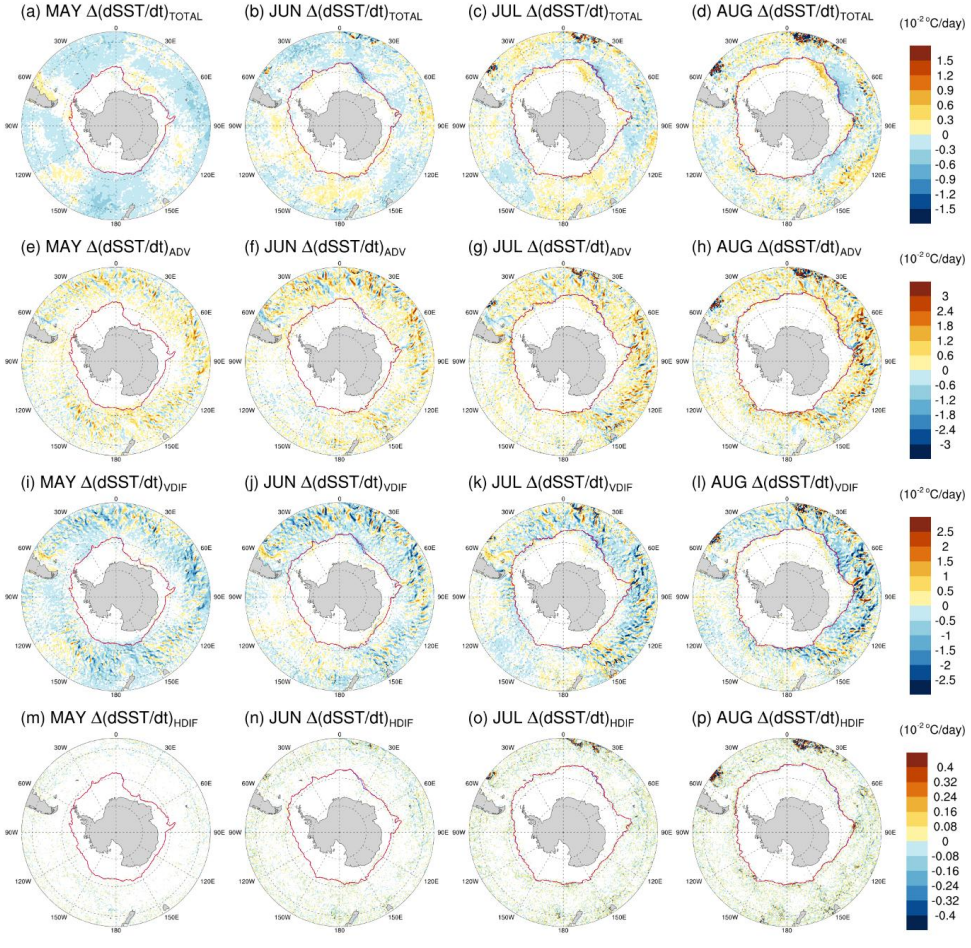


Figure 5 Monthly mean responses of net ocean surface heat flux, defined as FULL minus CTRL, and monthly mean spray-mediated heat fluxes in the FULL experiments from May to August. Panels show net ocean surface heat flux responses (a–d) for the NUD configuration, and (i–l) for the FREE configuration. Panels show spray-mediated heat fluxes (e–h) in Exp_FULL$_{NUD}$, and (m–p) in Exp_FULL$_{FREE}$. The 15% sea ice concentration contours from the CTRL experiment (blue) and the FULL experiment (red) are overlaid on each panel. All fluxes are defined as positive downward, and spray-mediated heat fluxes are weighted by the open-water fraction. Color ranges were determined from the 99th percentile of the absolute magnitude. For NUD-FREE paired variables, ranges were constrained to zero-symmetric integer multiples of a common reference scale.

Given the spatially heterogeneous relationship between the SST and F_{SHF} responses, particularly in the FREE configuration, we further examine the processes governing the SST

https://doi.org/10.5194/egusphere-2026-5582
Preprint. Discussion started: 11 November 2026
© Author(s) 2026. CC BY 4.0 License.

458 response using the SST tendency diagnostics described in Section 2.6. These diagnostics allow
459 us to separate the contributions from advection and diffusion and, within the vertical-diffusion
460 tendency, to distinguish the effects of net surface heat flux from those of vertical mixing.
461 Figures 6 and 7 show the SST-tendency responses associated with total advection (the sum of
462 horizontal and vertical advection), vertical diffusion, and horizontal diffusion in the NUD and
463 FREE configurations, respectively, while Figure 8 further decomposes the vertical-diffusion-
464 driven tendency into the contributions from net surface heat flux and vertical mixing.
465



466
467 Figure 6 Monthly mean responses of sea surface temperature (SST) tendencies, defined as
468 Exp_FULL$_{NUD}$ minus Exp_CTRL$_{NUD}$, from May to August. Panels show (a–d) total SST
469 tendency responses, (e–h) the total-advection-driven responses (the sum of horizontal and

https://doi.org/10.5194/egusphere-2026-5582
Preprint. Discussion started: 11 November 2026
© Author(s) 2026. CC BY 4.0 License.

vertical advection), (i–l) vertical-diffusion-driven responses, and (m–p) horizontal-diffusion-driven responses. The 15% sea ice concentration contours from Exp_CTRL$_{NUD}$ (blue) and Exp_FULL$_{NUD}$ (red) are overlaid on each panel. Color ranges were determined from the 99th percentile of the absolute magnitude.

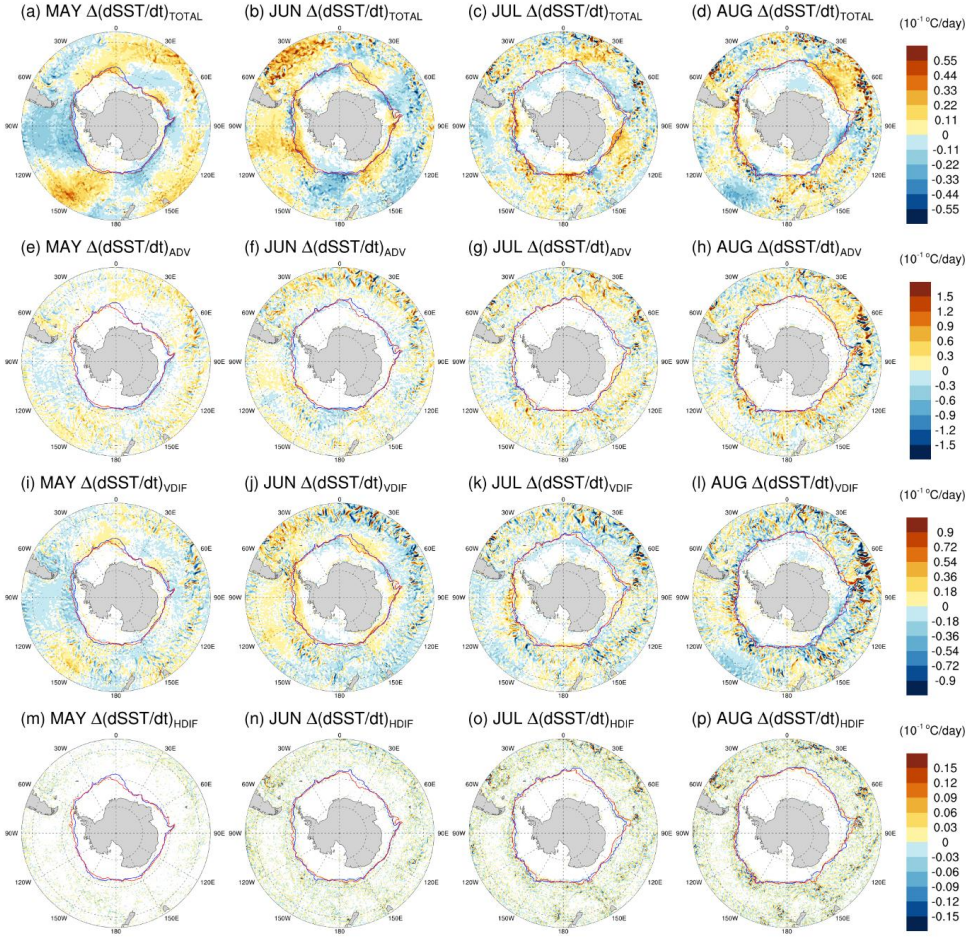


Figure 7 Same as Figure 6, but for the FREE configuration.

https://doi.org/10.5194/egusphere-2026-5582
Preprint. Discussion started: 11 November 2026
© Author(s) 2026. CC BY 4.0 License.

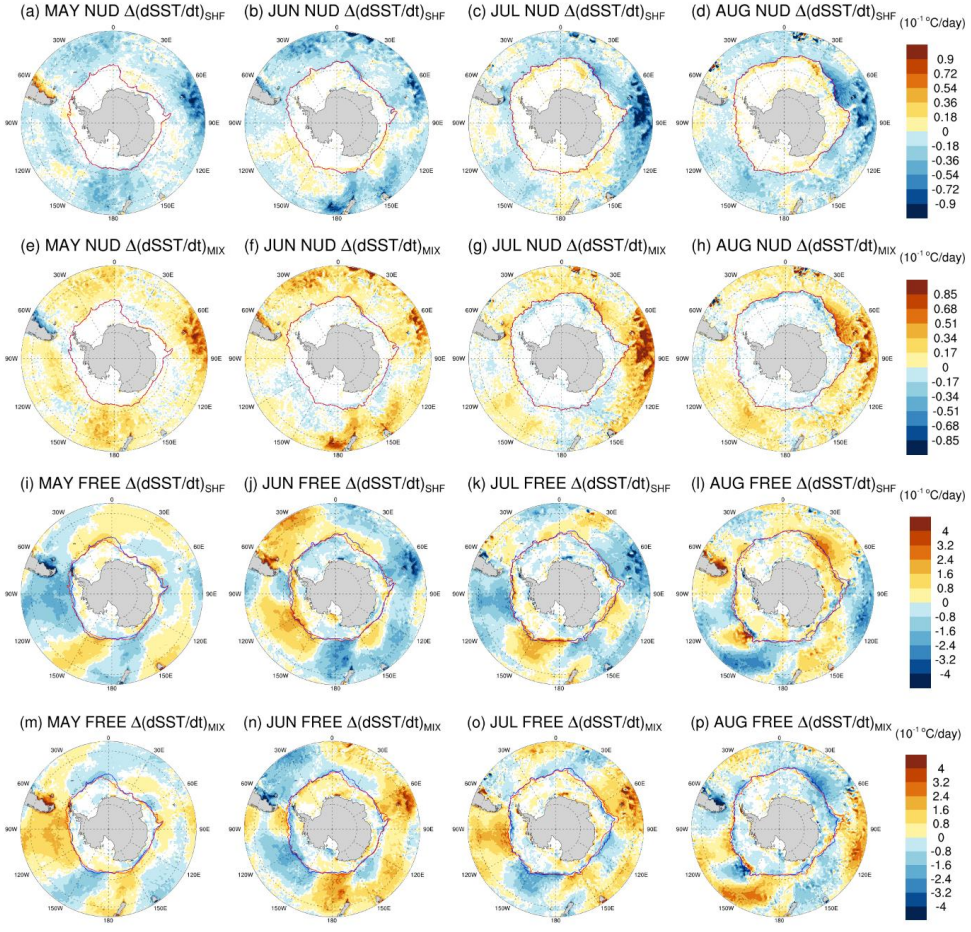


Figure 8 Monthly mean responses of decomposed vertical-diffusion-driven sea surface temperature (SST) tendencies, defined as FULL minus CTRL, from May to August. Panels show net-ocean-surface-heat-flux-driven responses (a–d) of the NUD configuration, and (i–l) of the FREE configuration. Panels show vertical-mixing-driven responses (e–h) of the NUD configuration, and (m–p) of the FREE configuration. The 15% sea ice concentration contours from CTRL (blue) and FULL (red) are overlaid on each panel. Color ranges were determined from the 99th percentile of the absolute magnitude.

In the NUD configuration, the advection and vertical-diffusion responses are the primary contributors to the total SST tendency response (Figs. 6a–l), whereas the horizontal-diffusion response remains negligible throughout the simulation (Figs. 6m–p). Although the advection and vertical-diffusion responses are comparable in magnitude, they generally have opposite

https://doi.org/10.5194/egusphere-2026-5582
Preprint. Discussion started: 11 November 2026
© Author(s) 2026. CC BY 4.0 License.

signs, and their relative contributions vary across different sectors of the Southern Ocean. Over much of the open Southern Ocean, advection tends to produce a positive SST tendency, while vertical diffusion produces an opposing negative tendency, resulting in substantial compensation between the two processes. Consequently, the total SST tendency response is considerably smaller in magnitude than either contribution individually. By July and August, the negative vertical-diffusion response becomes particularly pronounced in the 60°–120°E sector and locally exceeds the opposing advective contribution, yielding a negative total SST tendency response in regions where pronounced SST cooling develops (Figs. 4c–d and 6c–d, 6g–l). The relative importance of the two processes nevertheless varies spatially, indicating that the SST response is governed by their regional balance rather than by a single dominant process. The vertical-diffusion response can be further understood through its net-surface-heat-flux and vertical-mixing contributions (Fig. 8). As described in Section 2.6, the vertical-mixing response is defined as the residual after removing the net-surface-heat-flux contribution from the vertical-diffusion tendency. Its full-depth vertical integral is close to zero over most regions (Fig. S6), supporting its interpretation as vertical redistribution by KPP mixing rather than a net heat source or sink.

In the NUD configuration, the vertical-diffusion-driven SST tendency is dominated by the net-surface-heat-flux contribution, while vertical mixing generally provides a weaker, compensating response (Figs. 8a–h). The net-surface-heat-flux contribution is predominantly negative over the open ocean, consistent with enhanced upward ocean surface heat loss shown in Figure 5, whereas vertical mixing generally produces a compensating positive tendency. In the 60°–120°E sector, the negative net-surface-heat-flux contribution becomes particularly pronounced from June through August and locally exceeds the opposing vertical-mixing contribution, accounting for most of the negative vertical-diffusion tendency in this region.

The FREE configuration exhibits the same overall hierarchy of SST-tendency terms, with advection and vertical diffusion dominating over horizontal diffusion, but the responses are markedly larger and more spatially heterogeneous than in the NUD configuration (Figs. 6–7). As in the NUD configuration, the advection- and vertical-diffusion-driven tendencies

https://doi.org/10.5194/egusphere-2026-5582
Preprint. Discussion started: 11 November 2026
© Author(s) 2026. CC BY 4.0 License.

519 frequently oppose each other, although their relative magnitudes and signs vary strongly by
520 sector and month. Their incomplete compensation produces pronounced zonal variations in
521 total SST tendency response, particularly near the ice edge from June onward (Figs. 7b–l).
522 Although compensation between advection and vertical diffusion is common, the two
523 contributions also reinforce each other in some regions, further enhancing the local total SST
524 tendency response. For example, the positive SST tendency in the Weddell Sea in May and
525 June is associated with positive contributions from both advection and vertical diffusion (Figs.
526 7a–b, e–f, i–j). These spatially varying balances are consistent with contrasts between warming
527 and cooling in the FREE SST response (Figs. 4e–h). Thus, the NUD configuration provides an
528 approximation to the ocean–wave–sea ice response under prescribed atmospheric forcing,
529 whereas the FREE configuration additionally allows atmospheric circulation feedbacks that
530 amplify the SST-tendency response and enhance its regional variability. A similar
531 decomposition of vertical-diffusion tendency in the FREE configuration reveals much stronger
532 and more spatially heterogeneous contributions from both net surface heat flux and vertical
533 mixing (Figs. 8i–p). Unlike the relatively coherent compensation found in the NUD
534 configuration, the vertical-mixing response in the FREE configuration exhibits pronounced
535 zonal variations, with alternating positive and negative SST tendencies whose magnitude is
536 comparable to that of the net-surface-heat-flux contribution in many regions. The two
537 components frequently oppose each other, indicating that vertical redistribution substantially
538 modifies the SST tendency imposed by the surface heat-flux response rather than acting as a
539 secondary correction. This mixing contribution reflects changes in KPP vertical redistribution,
540 which in the FULL experiment includes Langmuir-mixing modification associated with surface
541 waves, together with adjustment arising from the evolving upper-ocean stratification and
542 atmospheric forcing. Consequently, the stronger SST response in the FREE configuration
543 reflects not only enhanced and spatially varying surface heat-flux forcing, but also its
544 interaction with a substantially reorganized vertical-mixing response.

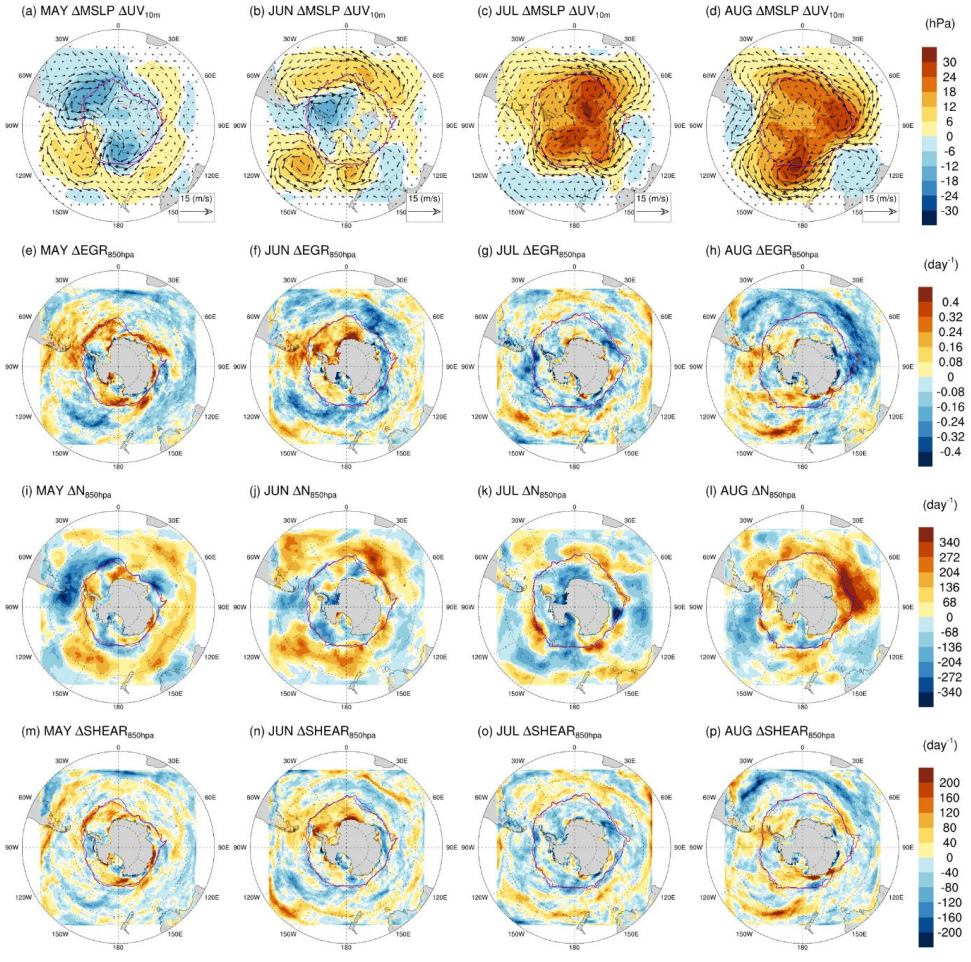
545 The stronger sea-ice, oceanic, and surface-flux responses in the FREE configuration
546 relative to the NUD configuration suggest that allowing the atmosphere to evolve interactively

https://doi.org/10.5194/egusphere-2026-5582
Preprint. Discussion started: 11 November 2026
© Author(s) 2026. CC BY 4.0 License.

introduces feedbacks that amplify the coupled response. Figure 9 therefore examines the associated near-surface atmospheric circulation responses and changes in the eddy growth rate (EGR; Simmonds and Lim, 2009), computed using the 900-, 850-, and 800-hPa levels, for the FREE configuration. Consistent with the pronounced zonal variability described above, the atmospheric-circulation responses in the FREE configuration becomes increasingly organized from June onward, with large-scale sea-level pressure anomalies producing sector dependent changes in near-surface winds along the ice edge (Figs. 9a–d). The near-surface wind responses are broadly consistent with the accompanying responses in sea-ice motion and dynamical SIC tendency, indicating a role for atmospheric circulation responses in modulating regional ice transport (Figs. 3i–l). The circulation response also contains meridional wind components, whose direction varies around the Southern Ocean and can alter the advection of relatively warm and moist or cold and dry air across the ice edge. These responses in near-surface temperature and humidity contrasts can locally enhance or suppress the air–sea thermodynamic disequilibrium, contributing to the alternating regions of enhanced upward and downward net ocean surface-flux responses seen in the FREE configuration (Figs. 5i–l). The atmospheric-circulation and EGR responses show partial spatial correspondence, with several of the larger EGR responses occurring in the vicinity of pronounced circulation responses, particularly from June onward (Figs. 9a–h). However, the correspondence is not spatially uniform, indicating that the circulation responses are not related to EGR responses in a simple one-to-one manner. Separating the EGR response into its stability and wind-shear components shows that the stability contribution is generally larger in magnitude and exhibits broader spatial structures, whereas the wind-shear contribution provides additional regional-scale modulation (Figs. 9i–p). Along portions of the open ocean near the ice edge, the stability response also shows some spatial correspondence with the large-scale circulation responses. When considered together with the SST and net ocean surface-flux responses (Figs. 4 and 5), these patterns are more appropriately interpreted as components of a coupled monthly-mean adjustment. In some regions, enhanced ocean-to-atmosphere heat loss coexists with SST cooling and reduced lower-level stability, reflecting the combined outcome of surface energy exchange and subsequent

https://doi.org/10.5194/egusphere-2026-5582
Preprint. Discussion started: 11 November 2026
© Author(s) 2026. CC BY 4.0 License.

575 oceanic and atmospheric adjustments rather than a simple local forcing-response relationship.
576 Thus, the stability-related EGR responses are consistent with a feedback pathway involving
577 surface heat exchange, SST, and lower-tropospheric adjustment, while the wind-shear response
578 further modulates the regional EGR structure. Because these diagnostics are based on monthly
579 means, however, they characterized the resulting coupled mean-state adjustment rather than
580 the temporal sequence of the underlying feedback processes.
581



582

583 Figure 9 Monthly mean responses of atmospheric circulation and eddy growth rate (EGR),
584 defined as Exp_FULL$_{FREE}$ minus Exp_CTRL$_{FREE}$, from May to August. Panels show (a–d)
585 atmospheric circulation responses, (e–h) EGR responses, (i–l) responses in the stability

https://doi.org/10.5194/egusphere-2026-5582
Preprint. Discussion started: 11 November 2026
© Author(s) 2026. CC BY 4.0 License.

component of EGR, and (m–p) responses in the wind-shear component of EGR. The 15% sea ice concentration contours from Exp_CTRL$_{FREE}$ (blue) and Exp_FULL$_{FREE}$ (red) are overlaid on each panel. Color ranges were determined from the 99th percentile of the absolute magnitude.

4. Conclusions and discussions

This study investigates the wave-induced atmosphere–ocean processes on Antarctic sea ice simulation using a regional atmosphere–ocean–wave–sea ice coupled model with newly implemented physical parameterizations. We conducted a series of pan-Antarctic experiments with different model configurations for the sea ice growth season of 2002, a period that included an explosive cyclone in the Ross Sea near the beginning of the simulation period. In particular, we examine the combined effects of spray-mediated heat flux and Langmuir mixing on Antarctic sea ice response under both atmosphere-nudged and fully coupled model configurations.

In regions of high wave activity, spray-mediated heat flux amplifies the total energy exchange between the atmosphere and the ocean through nonlinear interactions with interfacial heat fluxes, while Langmuir turbulence primarily enhances vertical mixing in the upper ocean. During the sea ice growth season, these processes produce distinct sea-ice and ocean responses that depend strongly on the model configuration. When atmospheric circulation is constrained by nudging, the responses of sea-ice and ocean are generally weak and spatially uniform across the Southern Ocean. In contrast, fully coupled simulations produce stronger and zonally heterogeneous responses, highlighting the importance of atmospheric feedbacks. In particular, changes in net ocean surface heat flux associated with spray-mediated heat transfer and Langmuir mixing modify low-level atmospheric stability and local circulation. These atmospheric adjustments, in turn, alter air–sea thermodynamic disequilibrium and feed back to the ocean surface heat budget. In addition, wave penetration into the ice-covered regions promotes spray-mediated heat fluxes and local supercooling, creating favorable conditions for new ice formation. These results suggest that penetrating waves affect sea ice not only directly through ice fracturing (e.g., Roach et al., 2019; Yang et al., 2024), but also indirectly by modifying the ocean thermal environment.

https://doi.org/10.5194/egusphere-2026-5582
Preprint. Discussion started: 11 November 2026
© Author(s) 2026. CC BY 4.0 License.

In our coupling framework, penetrating waves are primarily generated in the open ocean and then propagate into ice-covered regions, as illustrated during the explosive cyclone (Figs. S2–S3). However, wave energy may also be generated locally within partially ice-covered, fetch-limited regions, where the available open-water distance is constrained by sea ice. Such conditions differ from the open-water assumptions underlying classical wind-wave generation theories (e.g., Phillips, 1957; Miles, 1957) and from the standard source-term formulations used in third-generation wave models such as WW3 and SWAN. Although these models often account for partial ice cover by scaling wind input with the open-water fraction, recent studies suggest that wind input, wave growth, and wave attenuation in the marginal ice zone depend on more complex interactions among wind, waves, swell, and sea ice (e.g., Thomson, 2022). This limitation highlights the need for more physically based treatments of fetch-limited wave generation in ice-covered seas, particularly given the strong regional and seasonal variability of wave penetration into Antarctic ice margins (Fraser et al., 2026).

As discussed in Andreas et al. (2015), the sea spray generation function (SSGF) is a major source of uncertainty in estimates of spray-mediated heat flux. In addition to the SSGF of Zhao et al. (2024), we also tested the SSGF of Andreas (1998), which depends only on wind speed, using the setup of Exp_FULL$_{FREE}$. The spray-mediated heat fluxes calculated using the Andreas (1998) SSGF are about one-fifth of those obtained using the Zhao et al. (2024) SSGF (Fig. S7 in the Supplementary). Andreas (1998) was based on sea spray observations collected at an offshore site near the Dutch coast, around 52°N, during the HEXOS Main Experiment, whereas Zhao et al. (2024) fitted the SSGF using laboratory wave-tank measurements and selected environmental variables. It remains uncertain whether these data-fitted SSGFs predict realistic spray droplet concentrations and size distribution in polar environments, especially near the ice edge. Targeted observations of sea spray and key environmental variables in polar regions are therefore needed to better constrain empirical SSGFs. In addition to empirical formulations, physics-based SSGFs have also been developed, although they may be most applicable over limited droplet-size ranges. Deike et al. (2022) introduced a mechanistic SSGF that describes air-bubble entrainment by breaking waves, while Barr et al. (2023) used a sea-

https://doi.org/10.5194/egusphere-2026-5582
Preprint. Discussion started: 11 November 2026
© Author(s) 2026. CC BY 4.0 License.

state-dependent, wave-dissipation-based spume SSGF that links spray mass flux and size distribution to breaking-wave processes.

As a final note, this study is based on a case simulation during the sea ice growth season. It is likely that the sea-ice, ocean, and atmospheric responses related to wave-induced processes are seasonally and regionally dependent (e.g., Fraser et al. 2026). In addition, the pronounced reorganization of Antarctic sea ice after 2016 is possibly associated with the subsurface warming of the Southern Ocean (e.g., Purich and Doddrigde, 2023). Wave-induced processes, in particular wave-induced mixing, may affect sea ice and the ocean differently under different ocean thermal background states. Thus, it is essential to conduct additional simulations initialized in different seasons and years. Our coupled model has implemented prognostic floe size to represent direct wave–ice interactions (Yang et al., 2024), but this study does not consider that process. The simulated floe size requires longer-than-seasonal timescale to emerge because the initialization of floe size distribution is still based on a simple power-law due to the lack of observations. Future works will investigate both direct and indirect pathways of wave influences on Antarctic sea ice based on longer simulations.

https://doi.org/10.5194/egusphere-2026-5582
Preprint. Discussion started: 11 November 2026
© Author(s) 2026. CC BY 4.0 License.

Code and data availability: The pan-Antarctic simulation outputs and diagnostics analyzed in this study are archived in Zenodo repository: https://doi.org/10.5281/zenodo.22739312 (Yang, 2026).

Author contributions: CYY conducted numerical experiments, performed the analysis, and wrote the original manuscript. CYY implemented the physical parameterizations in the coupled model with the contribution from XX. CYY and JL were responsible for the conceptualization of this study and the revisions of the manuscript. All co-authors reviewed and commented on the final version of the manuscript.

Competing interests: The authors declare that they have no conflict of interest

Acknowledgements: This research is supported by the National Key Research and Development Project of China (2024YFF0506600), the National Natural Science Foundation of China (42376237, U2542215) and the Southern Marine Science and Engineering Guangdong Laboratory (Zhuhai) (SML2024SP023). We also acknowledge the high-performance computing support from the School of Atmospheric Science of Sun Yat-sen University.

https://doi.org/10.5194/egusphere-2026-5582
Preprint. Discussion started: 11 November 2026
© Author(s) 2026. CC BY 4.0 License.

5. References

Andreas, E. L.: Sea spray and the turbulent air-sea heat fluxes. *J. Geophys. Res.-Oceans*, 97(C7), 11429–11441. https://doi.org/10.1029/92JC00876, 1992.

Andreas, E. L.: A New Sea Spray Generation Function for Wind Speeds up to 32 m s^{-1}. *J. Phys. Oceanogr.*, 28, 2175–2184, https://doi.org/10.1175/1520-0485(1998)028<2175:ANSSGF>2.0.CO;2, 1998.

Andreas, E. L., Mahrt, L. and Vickers, D.: An improved bulk air–sea surface flux algorithm, including spray-mediated transfer. *Q. J. R. Meteorol. Soc.*, 141, 642–654. https://doi.org/10.1002/qj.2424, 2015.

Ardhuin, F., O'Reilly, W. C., Herbers, T. H. C., and Jessen, P. F.: Swell transformation across the continental shelf. Part I: Attenuation and directional broadening, *J. Phys. Oceanogr.*, 33, 1921–1939, https://doi.org/10.1175/1520-0485(2003)033<1921:STATCS>2.0.CO;2, 2003.

Ardhuin, F., Rogers, W. E., Babanin, A. V., Filipot, J., Magne, R., Roland, A., van der Westhuysen, A., Queffeulou, P., Lefevre, J., Aouf, L., and Collard, F.: Semiempirical dissipation source functions for ocean waves. Part I: Definition, calibration, and validation, *J. Phys. Oceanogr.*, 40, 1917–1941, https://doi.org/10.1175/2010JPO4324.1, 2010.

Ardhuin, F., and Roland, A.: Coastal wave reflection, directional spread, and seismoacoustic noise sources, *J. Geophys. Res.-Oceans*, 117, C00J20, https://doi.org/10.1029/2011JC007832, 2012.

Babanin, A. V., and Haus, B. K.: On the existence of water turbulence induced by nonbreaking surface waves. *J. Phys. Oceanogr.*, 39(10), 2675–2679. https://doi.org/10.1175/2009JPO4202.1, 2009.

Barr, B. W., Chen, S. S., and Fairall, C. W.: Sea-state-dependent sea spray and air–sea heat fluxes in tropical cyclones: A new parameterization for fully coupled atmosphere–wave–ocean models. *J. Atmos. Sci.*, 80(4), 933–960. https://doi.org/10.1175/JAS-D-22-0126.1, 2023.

https://doi.org/10.5194/egusphere-2026-5582
Preprint. Discussion started: 11 November 2026
© Author(s) 2026. CC BY 4.0 License.



706 Battjes, J. A. and Janssen, J. P. F. M.: Energy loss and set-up due to breaking of random waves,
707 *Proc. 16th Int. Conf. Coastal Engineering*, ASCE, 569–587,
708 https://doi.org/10.1061/9780872621909.034, 1978.
709 Boutin, G., Lique, C., Ardhuin, F., Rousset, C., Talandier, C., Accensi, M., and Girard-Ardhuin,
710 F.: Towards a coupled model to investigate wave–sea ice interactions in the Arctic
711 marginal ice zone, *The Cryosphere*, 14, 709–735, https://doi.org/10.5194/tc-14-709-2020,
712 2020.
713 Briegleb, B. P. and Light, B.: A Delta-Eddington multiple scattering parameterization for solar
714 radiation in the sea ice component of the Community Climate System Model. (No.
715 NCAR/TN-472+STR). University Corporation for Atmospheric Research,
716 https://doi.org/10.5065/D6B27S71, 2007.
717 Cavaleri, L., and Malanotte-Rizzoli, P.: Wind-wave prediction in shallow water: Theory and
718 applications., *J. Geophys. Res.-Oceans*, 86, 10961–10973,
719 https://doi.org/10.1029/JC086iC11p10961, 1981.
720 Chen, F. and Dudhia, J.: Coupling an advanced land surface–hydrology model with the Penn
721 State–NCAR MM5 modeling system. Part I: Model implementation and sensitivity. *Mon.
722 Wea. Rev.*, 129, 569–585, https://doi.org/10.1175/1520-
723 0493(2001)129<0569:CAALSH>2.0.CO;2, 2001.
724 Collins, W. D., Rasch, P. J., Boville, B. A., McCaa, J., Williamson, D. L., Kiehl, J. T., Briegleb,
725 B. P., Bitz, C., Lin, S.-J., Zhang, M., and Dai, Y.: Description of the NCAR Community
726 Atmosphere Model (CAM 3.0). (No. NCAR/TN-464+STR). University Corporation for
727 Atmospheric Research. https://doi.org/10.5065/D63N21CH, 2004.
728 D'Asaro, E. A.: Turbulence in the upper-ocean mixed layer. *Annu. Rev. Mar. Sci.*, 6, 101–115.
729 https://doi.org/10.1146/annurev-marine-010213-135138, 2014.
730 Deike, L., Reichl, B. G., and Paulot, F.: A mechanistic sea spray generation function based on
731 the sea state and the physics of bubble bursting. *AGU Advances*, 3, e2022AV000750.
732 https://doi.org/10.1029/2022AV000750, 2022.

https://doi.org/10.5194/egusphere-2026-5582
Preprint. Discussion started: 11 November 2026
© Author(s) 2026. CC BY 4.0 License.

Drennan, W. M., Graber, H. C., Hauser, D., and Quentin, C.: On the wave age dependence of wind stress over pure wind seas. *J. Geophys. Res.-Oceans*, 108(C3), 8062. https://doi.org/10.1029/2000JC000715, 2003.

Erikson, L. H., Morim, J., Hemer, M., Young, I., Wang, X. L., Mentaschi, L., Mori, N., Semedo, A., Stopa, J., Grigorieva, V., Gulev, S., Aarnes, O., Bidlot, J.-R., Breivik, Ø., Bricheno, L., Shimura, T., Menendez, M., Markina, M., Sharmar, V., Trenham, C., Wolf, J., Appendini, C., Caires, S., Groll, N., and Webb, A.: Global ocean wave fields show consistent regional trends between 1980 and 2014 in a multi-product ensemble. *Commun. Earth Environ.*, 3, 320. https://doi.org/10.1038/s43247-022-00654-9, 2022.

Fairall, C. W., Bradley, E. F., Hare, J. E., Grachev, A. A., and Edson, J. B.: Bulk Parameterization of Air–Sea Fluxes: Updates and Verification for the COARE Algorithm. *J. Climate*, 16(4), 571–591, https://doi.org/10.1175/1520-0442(2003)016<0571:BPOASF>2.0.CO;2, 2003.

Fraser, A. D., Day, N., Wang, Z., Bennetts, L. G., Liu, Q., O'Farrell, S., Coleman, R., Voermans, J., Xu, S., Zhu, W., Auger, M., Massom, R. A., Wongpan, P., Craw, L., Brouwer, J., Toyota, T., Heil, P., and Horvat, C.: Revealing the Antarctic marginal ice zone with a decade-long wave-in-ice climatology. *Nat. Commun.*, 17, 6648 (2026). https://doi.org/10.1038/s41467-026-73203-z, 2026.

Freitas, S. R., Grell, G. A., Molod, A., Thompson, M. A., Putman, W. M., Santos e Silva, C. M. and Souza, E. P.: Assessing the Grell–Freitas convection parameterization in the NASA GEOS modeling system. *J. Adv. Model. Earth Syst.*, 10, 1266–1289, https://doi.org/10.1029/2017MS001251, 2018.

Guan, C., and Xie, L.: On the Linear Parameterization of Drag Coefficient over Sea Surface. *J. Phys. Oceanogr.*, 34(12), 2847–2851. https://doi.org/10.1175/JPO2664.1, 2004.

Harcourt, R. R., and D'Asaro, E. A.: Large-eddy simulation of Langmuir turbulence in pure wind seas. *J. Phys. Oceanogr.*, 38(7), 1542–1562. https://doi.org/10.1175/2007jpo3842.1, 2008.

https://doi.org/10.5194/egusphere-2026-5582
Preprint. Discussion started: 11 November 2026
© Author(s) 2026. CC BY 4.0 License.

760 Hasselmann, S., Hasselmann, K., Allender, J. H., and Barnett, T. P.: Computations and
761 parameterizations of the nonlinear energy transfer in a gravity-wave spectrum, Part II:
762 Parameterizations of the nonlinear energy transfer for application in wave models, *J. Phys.*
763 *Oceanogr.*, 15, 1378–1391, https://doi.org/10.1175/1520-
764 0485(1985)015<1378:CAPOTN>2.0.CO;2, 1985.
765 Hersbach, H., Bell, B., Berrisford, P., Biavati, G., Horányi, A., Muñoz Sabater, J., Nicolas, J.,
766 Peubey, C., Radu, R., Rozum, I., Schepers, D., Simmons, A., Soci, C., Dee, D., Thépaut,
767 J-N.: ERA5 hourly data on single levels from 1940 to present, *Copernicus Climate*
768 *Change Service (C3S) Climate Data Store (CDS) [data set]*,
769 https://doi.org/10.24381/cds.adbb2d47, 2023.
770 Horvat, C. and Tziperman, E.: A prognostic model of the sea-ice floe size and thickness
771 distribution, *The Cryosphere*, 9, 2119–2134, https://doi.org/10.5194/tc-9-2119-2015,
772 2015.
773 Hunke, E. C. and Dukowicz, J. K.: An elastic-viscous-plastic model for sea ice dynamics. *J.*
774 *Phys. Oceanogr.*, 27, 1849–67, https://doi.org/10.1175/1520-
775 0485(1997)027<1849:AEVPMF>2.0.CO;2, 1997.
776 Hunke, E. C., Hebert, D. A., and Lecomte, O.: Level-ice melt ponds in the Los Alamos Sea Ice
777 Model, CICE. *Ocean Model.*, 71, 26–42, https://doi.org/10.1016/j.ocemod.2012.11.008,
778 2013.
779 Kohout, A. L., Williams, M. J. M., Dean, S. M., and Meylan, M. H.: Storm-induced sea-ice
780 breakup and the implications for ice extent. *Nature*, 509, 604–607.
781 https://doi.org/10.1038/nature13262, 2014.
782 Kumar, N., Voulgaris, G., Warner, J. C., and Olabarrieta, M.: Implementation of the vortex
783 force formalism in the coupled ocean-atmosphere-wave-sediment transport (COAWST)
784 modeling system for inner shelf and surf zone applications, *Ocean Model.*, 47, 65-95,
785 https://doi.org/10.1016/j.ocemod.2012.01.003, 2012.
786 Laloue, A., Ghantous, M., Faugère, Y., Dalphinet, A., and Aouf, L.: Statistical analysis of global
787 ocean significant wave heights from satellite altimetry over the past 2 decades, in: 8th

https://doi.org/10.5194/egusphere-2026-5582
Preprint. Discussion started: 11 November 2026
© Author(s) 2026. CC BY 4.0 License.

edition of the Copernicus Ocean State Report (OSR8), edited by: von Schuckmann, K., Moreira, L., Grégoire, M., Marcos, M., Staneva, J., Brasseur, P., Garric, G., Lionello, P., Karstensen, J., and Neukermans, G., Copernicus Publications, State Planet, 4-osr8, 6, https://doi.org/10.5194/sp-4-osr8-6-2024, 2024.

Large, W. G., McWilliams, J. C., and Doney, S. C.: Oceanic vertical mixing: A review and a model with a nonlocal boundary layer parameterization. *Rev. Geophys.*, 32(4), 363–403, https://doi.org/10.1029/94RG01872, 1994.

Li, Q., Webb, A., Fox-Kemper, B., Craig, A., Danabasoglu, G., Large, W. G., and Vertenstein, M.: Langmuir mixing effects on global climate: WAVEWATCH III in CESM. *Ocean Model.*, 103, 145–160. https://doi.org/10.1016/j.ocemod.2015.07.020, 2016.

Li, S., Babanin, A., Liu, Q., Liu, J., Li, R., and Voermans, J.: Effect of ocean surface waves on sea ice using coupled wave–ice–ocean modelling. *Ocean Model.*, 196, 102540. https://doi.org/10.1016/j.ocemod.2025.102540, 2025.

McWilliams, J. C., Sullivan, P. P., and Moeng, C.-H.: Langmuir turbulence in the ocean. *J. Fluid Mech.*, 334, 1–30. https://doi.org/10.1017/S0022112096004375, 1997.

McWilliams, J. C., and Sullivan, P. P.: Vertical mixing by Langmuir circulations. *Spill Sci. Technol. Bull.*, 6(3–4), 225–237. https://doi.org/10.1016/S1353-2561(01)00041-X, 2000.

McWilliams, J. C., Sullivan, P. P., and Moeng, C.-H.: Langmuir turbulence in the ocean. *J. Fluid Mech.*, 334, 1–30. https://doi.org/10.1017/s0022112096004375, 1997.

Miles, J. W.: On the generation of surface waves by shear flows. *J. Fluid Mech.*, 3(2), 185–204, https://doi.org/10.1017/S0022112057000567, 1957.

Menemenlis, D., Campin, J. M., Heimbach, P., Hill, C., Lee, T., Nguyen, A., Schodlok, M., and Zhang, H.: ECCO2: High resolution global ocean and sea ice data synthesis, *Mercator Ocean Quarterly Newsletter*, 31, 13–21, https://www.mercator-ocean.eu/wp-content/uploads/2015/06/lettre_31_en.pdf (last access: 15 September 2026), 2008.

Morrison, H., Thompson, G., and Tatarskii, V.: Impact of Cloud Microphysics on the Development of Trailing Stratiform Precipitation in a Simulated Squall Line: Comparison

https://doi.org/10.5194/egusphere-2026-5582
Preprint. Discussion started: 11 November 2026
© Author(s) 2026. CC BY 4.0 License.

of One– and Two–Moment Schemes. *Mon. Wea. Rev.*, 137, 991–1007. https://doi.org/10.1175/2008MWR2556.1, 2009.

Nakanishi, M., and Niino., H.: Development of an improved turbulence closure model for the atmospheric boundary layer. *J. Meteor. Soc. Japan*, 87, 895–912, https://doi.org/10.2151/jmsj.87.895, 2009.

Notz, D., McPhee, M. G., Worster, M. G., Maykut, G. A., Schlünzen, K. H., and Eicken, H.: Impact of underwater-ice evolution on Arctic summer sea ice, *J. Geophys. Res.-Oceans*, 108, 3223, https://doi.org/10.1029/2001JC001173, 2003.

Notz, D., Jahn, A., Holland, M., Hunke, E., Massonnet, F., Stroeve, J., Tremblay, B., and Vancoppenolle, M.: The CMIP6 Sea-Ice Model Intercomparison Project (SIMIP): understanding sea ice through climate-model simulations, *Geosci. Model Dev.*, 9, 3427–3446, https://doi.org/10.5194/gmd-9-3427-2016, 2016.

Parkinson, C. L.: A 40-y record reveals gradual Antarctic sea ice increases followed by decreases at rates far exceeding the rates seen in the Arctic, *Proc. Natl. Acad. Sci. U.S.A.,* 116 (29), 14414-14423, https://doi.org/10.1073/pnas.1906556116, 2019.

Phillips, O. M.: On the generation of waves by turbulent wind. *J. Fluid Mech.*, 2(5), 417–445, https://doi.org/10.1017/S0022112057000233, 1957.

Purich, A., and Doddridge, E. W.: Record low Antarctic sea ice coverage indicates a new sea ice state. *Commun. Earth Environ.*, 4, 314. https://doi.org/10.1038/s43247-023-00961-9, 2023.

Qiao, F., Yuan, Y., Yang, Y., Zheng, Q., Xia, C., and Ma, J.: Wave-induced mixing in the upper ocean: Distribution and application to a global ocean circulation model. *Geophys. Res. Lett.*, 31, L11303. https://doi.org/10.1029/2004GL019824, 2004.

Raphael, M. N., Maierhofer, T. J., Fogt, R. L., Hobbs, W. R., and Handcock, M. S.: A twenty-first century structural change in Antarctica's sea ice system. *Commun. Earth Environ.*, 6, 131. https://doi.org/10.1038/s43247-025-02107-5, 2025.

https://doi.org/10.5194/egusphere-2026-5582
Preprint. Discussion started: 11 November 2026
© Author(s) 2026. CC BY 4.0 License.

Roach, L. A., Bitz, C. M., Horvat, C., and Dean, S. M.: Advances in modeling interactions between sea ice and ocean surface waves. *J. Adv. Model. Earth Sy.*, 11, 4167–4181. https://doi.org/10.1029/2019MS001836, 2019.

Shchepetkin, A. F., and McWilliams, J. C.: The Regional Ocean Modeling System: A split-explicit, free-surface, topography following coordinates ocean model, *Ocean Model.*, 9, 347-404, https://doi.org/10.1016/j.ocemod.2004.08.002, 2005.

Shi, R., Xu, F., Liu, L., Fan, Z., Yu, H., Li, H., Li, X., and Zhang, Y.: The effects of ocean surface waves on global intraseasonal prediction: Case studies with a coupled CFSv2.0–WW3 system. *Geosci. Model Dev.*, 15, 2345–2363. https://doi.org/10.5194/gmd-15-2345-2022, 2022.

Shi, X., Notz, D., Liu, J., Yang, H., and Lohmann, G.: Sensitivity of Northern Hemisphere climate to ice–ocean interface heat flux parameterizations, *Geosci. Model Dev.*, 14, 4891–4908, https://doi.org/10.5194/gmd-14-4891-2021, 2021.

Simmonds, I., and Lim, E.-P.: Biases in the calculation of Southern Hemisphere mean baroclinic eddy growth rate. *Geophys. Res. Lett.*, 36(1), L01707. https://doi.org/10.1029/2008GL036320, 2009.

Smyth, W. D., Skyllingstad, E. D., Crawford, G. B., Wijesekera, H.: Nonlocal fluxes and Stokes drift effects in the K-profile parameterization. Ocean Dyn. 52, 104–115. https://doi.org/10.1007/s10236-002-0012-9, 2002.

Song, Y., Qiao, F., Liu, J., Shu, Q., Bao, Y., Wei, M., and Song, Z.: Effects of sea spray on large-scale climatic features over the Southern Ocean. *J. Climate*, 35(14), 4645–4663. https://doi.org/10.1175/JCLI-D-21-0608.1, 2022.

Sullivan, P. P., and McWilliams, J. C.: Dynamics of winds and currents coupled to surface waves. *Annu. Rev. Fluid Mech.*, 42, 19–42. https://doi.org/10.1146/annurev-fluid-121108-145541, 2010.

Taylor, P. K., and Yelland, M. J.: The dependence of sea surface roughness on the height and steepness of the waves. *J. Phys. Oceanogr.,* 31, 572–590, https://doi.org/10.1175/1520-0485(2001)031<0572:TDOSSR>2.0.CO;2, 2001.

https://doi.org/10.5194/egusphere-2026-5582
Preprint. Discussion started: 11 November 2026
© Author(s) 2026. CC BY 4.0 License.



869 Terray, E. A., Donelan, M. A., Agrawal, Y. C., Drennan, W. M., Kahma, K. K., Williams, A. J.,
870 III, Hwang, P. A., & Kitaigorodskii, S. A.: Estimates of kinetic energy dissipation under
871 breaking waves. *J. Phys. Oceanogr.*, 26(5), 792–807. https://doi.org/10.1175/1520-
872 0485(1996)026<0792:EOKEDU>2.0.CO;2, 1996.
873 Thomson, J.: Wave propagation in the marginal ice zone: connections and feedback
874 mechanisms within the air-ice-ocean system. *Phil. Trans. R. Soc. A*, 380 (2235): 20210251
875 https://doi.org/10.1098/rsta.2021.0251, 2022.
876 Toba, Y., Komori, S., Suzuki, Y., and Zhao, D.: Similarity and dissimilarity in air–sea
877 momentum and CO_2 transfers: The nondimensional transfer coefficients in light of
878 windsea Reynolds number, in: Atmosphere–Ocean Interactions, Vol. II, edited by: Perrie,
879 W., 53–82, WIT Press, Southampton, https://doi.org/10.2495/978-1-85312-929-2/03,
880 2006.
881 Tolman, H. L.: Effects of numerics on the physics in a third-generation wind-wave model, *J.*
882 *Phys. Oceanogr.*, 22, 1095–1111, https://doi.org/10.1175/1520-
883 0485(1992)022<1095:EONOTP>2.0.CO;2, 1992.
884 Turner, A. K., Hunke, E. C., and Bitz, C. M.: Two modes of sea-ice gravity drainage: A
885 parameterization for large-scale modeling, *J. Geophys. Res.-Oceans*, 118, 2279–2294,
886 https://doi.org/10.1002/jgrc.20171, 2013.
887 Uchiyama, Y., McWilliams, J. C., and Shchepetkin, A. F.: Wave–current interaction in an
888 oceanic circulation model with a vortex force formalism: Application to the surf zone,
889 Ocean Model., 34, 16–35, https://doi.org/10.1016/j.ocemod.2010.04.002, 2010.
890 Umlauf, L. and Burchard, H.: A generic length-scale equation for geophysical turbulence
891 models, *J. Mar. Res.*, 61, 235–265, https://doi.org/10.1357/002224003322005087, 2003.
892 Van Roekel, L. P., Foxkemper, B., Sullivan, P. P., Hamlington, P. E., and Haney, S.: The form
893 and orientation of Langmuir cells for misaligned winds and waves, *J. Geophys. Res.-*
894 *Oceans*, 117, C05001, https://doi.org/10.1029/2011JC007516, 2012.
895 Veron, F.: Ocean spray. *Annu. Rev. Fluid Mech.*, 47, 507–538. https://doi.org/10.1146/annurev-
896 fluid-010814-014651, 2015.

https://doi.org/10.5194/egusphere-2026-5582
Preprint. Discussion started: 11 November 2026
© Author(s) 2026. CC BY 4.0 License.

Wang, P., McWilliams, J. C., Yuan, J., and Liang, J.-H.: Langmuir mixing schemes based on a modified K-profile parameterization. *J. Adv. Model. Earth Sy.*, 17, e2024MS004729. https://doi.org/10.1029/2024MS004729, 2025.

Xu, X., Liu, J., Yang, C.-Y., Huang, G., and Song, M.: The impacts of an explosive cyclone on the upper ocean and sea ice over the Southern Ocean based on numerical modeling results. *J. Geophys. Res.-Oceans*, 130, e2024JC022064. https://doi.org/10.1029/2024JC022064, 2025.

Yang, C.-Y., Liu, J., and Chen, D.: Understanding the influence of ocean waves on Arctic sea ice simulation: a modeling study with an atmosphere–ocean–wave–sea ice coupled model, *The Cryosphere*, 18, 1215–1239, https://doi.org/10.5194/tc-18-1215-2024, 2024.

Yang, C.-Y.: The simulated outputs and diagnostics analyzed in the manuscript: "Wave-induced atmosphere–ocean processes and their effects on Antarctic sea ice: A case study with an atmosphere–ocean–wave–sea ice coupled model", *Zenodo [data set]*, https://doi.org/10.5281/zenodo.22739312, 2026.

Yang, C.-Y., Gu, F., Liu, J., Rinke, A., Yang, H., and Shi, X.: Conservation of Heat in the Coupled Arctic Prediction System (CAPS v1.1): Comprehensive model evaluation based on the MOSAiC observations, *EGUsphere [preprint]*, https://doi.org/10.5194/egusphere-2026-362, 2026.

Young, I. R., and Ribal, A.: Multiplatform evaluation of global trends in wind speed and wave height. *Science*, 364, 548–552. https://doi.org/10.1126/science.aav9527, 2019.

Zhao Z., Shi, J., Wang, H., Yi, Z., Zhang, W., and Zhang, X.: Parameterization scheme of the sea surface drag coefficient considering the influence of wave states and sea spray stress. *Front. Mar. Sci.*, 11:1336709, https://doi.org/10.3389/fmars.2024.1336709, 2024.